CHALMERS
UNIVERSITY OF TECHNOLOGY

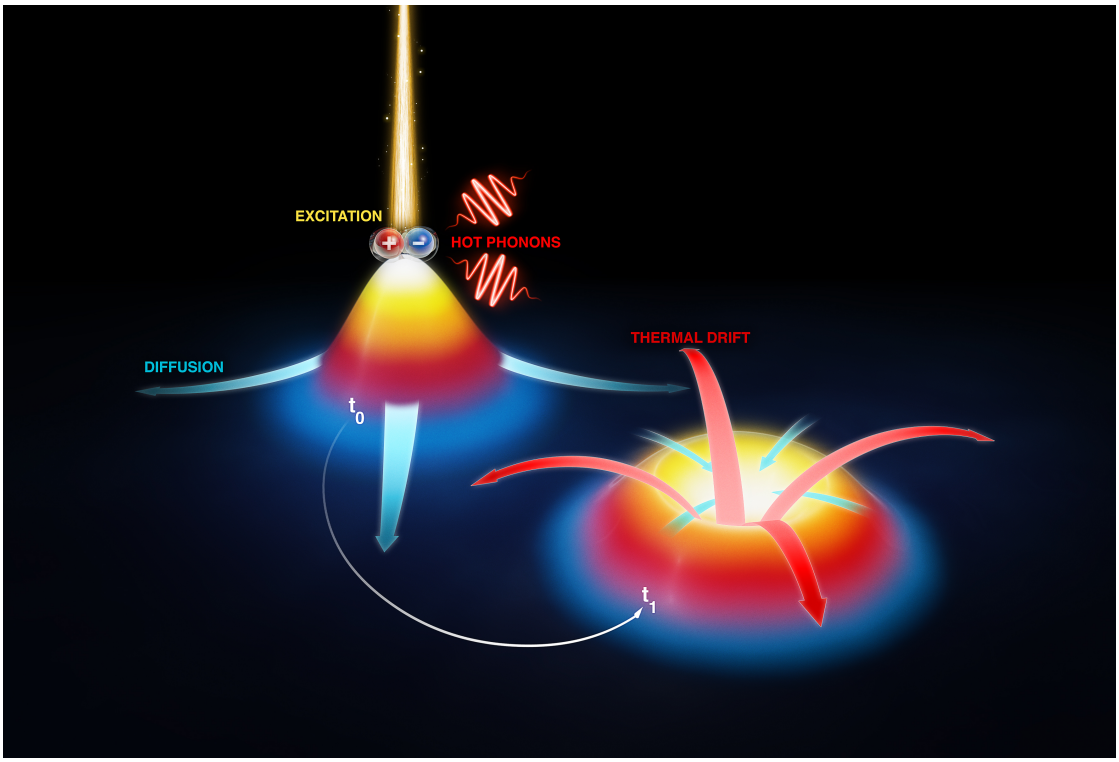


# Microscopic modeling of exciton diffusion and pump-probe spectroscopy in atomically thin materials

Master's thesis in Nanotechnology

Raül Perea Causín

Department of Physics
Chalmers University of Technology
Göteborg, Sweden 2019

Master's thesis 2019

# Microscopic modeling of exciton diffusion and pump-probe spectroscopy in atomically thin materials

Raül Perea Causín


CHALMERS

Department of Physics
Chalmers University of Technology
Göteborg, Sweden 2019

Microscopic modeling of exciton diffusion and pump-probe spectroscopy in atomically thin materials
**Author:** Raül Perea Causín



**Supervisor:** Samuel Brem
**Examiner:** Ermin Malic

Department of Physics
Chalmers University of Technolofy
SE-412 96 Göteborg
Sweden
Telephone + 46 (0)31-772 1000

Cover: Illustration of the exciton spatio-temporal dynamics and the formation of excitonic halos.

Göteborg, Sweden 2019

*A la Gemma,*
*als meus pares i*
*al meu germà*

# Abstract

Due to the reduced dielectric screening in two-dimensional materials, transition metal dichalcogenides (TMDs) exhibit a strong Coulomb interaction that leads to the formation of excitons (bound electron-hole pairs) with binding energies in the order of hundreds of meV. Therefore, excitonic effects dominate the physical properties of these materials even at room temperature. Due to their impressive properties, TMDs are suitable candidates for novel optoelectronic devices. For a better understanding of these materials it is necessary to investigate the microscopic mechanisms behind basic phenomena such as optical excitation, energy relaxation, and transport. To this end, a fully quantum-mechanical theoretical framework based on density matrix theory is presented in this thesis in order to address two fundamental questions: (1) the effect of excitation density on the excitonic and optical properties of TMDs, and (2) exciton spatial diffusion and the appearance of excitonic halos under strong excitation.

To find the effect of carrier density on the coherent excitonic states and the optical properties of the material, semiconductor Bloch equations are combined with the Wannier equation. Using this approach, it is found that exciton properties are significantly altered and even suppressed at high carrier densities due to dielectric many-particle screening and Pauli blocking. In the first part of this thesis, pump-probe experiments are modeled to provide a microscopic understanding of experimental observations of these phenomena.

Moreover, the Wigner representation is introduced to study the spatio-temporal dynamics of incoherent exciton populations and, specifically, the effect of excitation density on exciton diffusion. While under a weak excitation exciton diffusion follows the conventional Fick law, the results presented in this thesis show that under strong excitation a significant temperature gradient is created in the excitonic system, leading to the formation of spatial excitonic halos. This work unveils the microscopic mechanisms responsible for this unconventional phenomenon that was experimentally observed very recently.

**Keywords:** excitons, electrons, phonons, diffusion, propagation, optical absorption, density matrix formalism, Bloch equations.

# Acknowledgements

First, I would like to acknowledge Ermin and Samuel, my examiner and supervisor, respectively, who initated me in this field and taught me so much.

I am very grateful to Alexey Chernikov, Marvin Kulig, Jonas Zipfel and Jonas Ziegler (Regensburg, Germany) for measuring the excitonic halos and collaborating with us to find out the mechanisms responsible for these intriguing phenomena.

I want to acknowledge my current and previous colleagues: Maja, Samuel, Roberto, Simon, Roland, August, Magdulin, Zahra, and Iván.

And specially, thanks to my family, my friends, and to Gemma, for being always there.

# Contents

# Chapter 1

# Introduction

In the last decades there has been a clear trend into miniaturization of technological devices. However, classical materials used over the last century fail to operate at the narrow nanoscales that technology is reaching nowadays. In this sense, the experimental isolation and characterization of graphene in 2004 [1], which resulted in extense studies of this exceptional material over the following years, was very promising for future technological applications at the nanoscale [2]. Besides graphene, a vast amount of other atomically-thin two-dimensional materials have been experimentally realized and studied in the recent years [3–6]. Among them, semiconductor transition metal dichalcogenides have excelled as promising candidates for optoelectronic applications [7, 8].

Transition metal dichalcogenides (TMDs) are atomically-thin two-dimensional semiconductors. They are formed by a layer of transition metal atoms sandwiched between two layers of chalcogen atoms (c.f. figure 1.1a), with their chemical nomenclature being $MX_2$, with $M = Mo, W$ and $X = S, Se$. Their crystalline structure is hexagonal – as in graphene. However, while graphene is a semimetal with zero bandgap, the inversion symmetry in TMDs is broken and hence these materials have a bandgap. Even more interestingly, the indirect bandgap of bulk TMDs evolves into a direct bandgap in monolayer TMDs which is in the visible/infrared optical range (c.f. figure 1.1c). Furthermore, the optical emission of these materials is enhanced in monolayers with respect to bulk (c.f. figure 1.1d). The enhancement of the optical response is produced by excitonic effects that become very significant due to the reduced dielectric screening in two-dimensional structures. The reduced dielectric screening results in a strong Coulomb interaction through which electrons and holes are tightly bound, forming quasiparticles known as excitons (correlated electron-hole pairs). Accordingly, the peak observed in the optical response corresponds to the resonance energy of the lowest excitonic state. Flexibility, direct bandgap, and strong optical response – among others – make TMDs very promising for optoelectronic applications. In order to advance

in the implementation of these materials in real devices it is necessary to investigate fundamental phenomena that is expected to be very important for the correct understanding and control of these devices.

In this thesis, two fundamental questions regarding the optoelectronic operation of TMDs are addressed. The first one concerns the effect that a finite charge-carrier density has on the excitonic properties and, consequently, on the optical response of TMDs. Due to many-particle dielectric screening and Pauli-blocking, carrier density is expected to significantly alter the excitonic properties [10–13]. In this thesis it is shown how these properties are altered and a microscopic theoretical framework is provided in order to model experimental pump-probe measurements.

The second question addressed here corresponds to a phenomenon that is fundamental for understanding exciton transport: diffusion. Despite its importance, exciton diffusion has been little explored in experiments, with most studies focusing on low excitation densities [14–19] and only one recent study focusing on the density-dependence of exciton diffusion, showing intriguing halos in the photoluminescence at high densities [20]. There has only been one attempt to provide a theoretical explanation of this interesting phenomenon, which focuses on phonon wind and drag of excitons and is expected to work only at low temperatures [21], while the work by Kulig et al. has been performed at room temperature. In this thesis, a quantum-mechanical model is presented that can explain and predict the formation of spatial halos in the photoluminescence at high excitation and room temperature. In collaboration with the group of Alexey Chernikov (Regensburg, Germany), the theoretical predictions are compared with experimental observations to confirm the correctness of this theory.

The outline of this thesis is as follows. First, the theoretical framework will be presented, with exemplary figures showing a solution for the Bloch equations (to illustrate optical excitation and thermalization through scattering with phonons) and the excitonic wavefunctions, binding energies and optical absorption spectra. Afterwards, the results for both fundamental questions addressed here (density-dependence of optical absorption and exciton diffusion) will be presented and discussed. Finally, the conclusions of this work will be presented, with a summary of this project and suggestions for future work following this research.

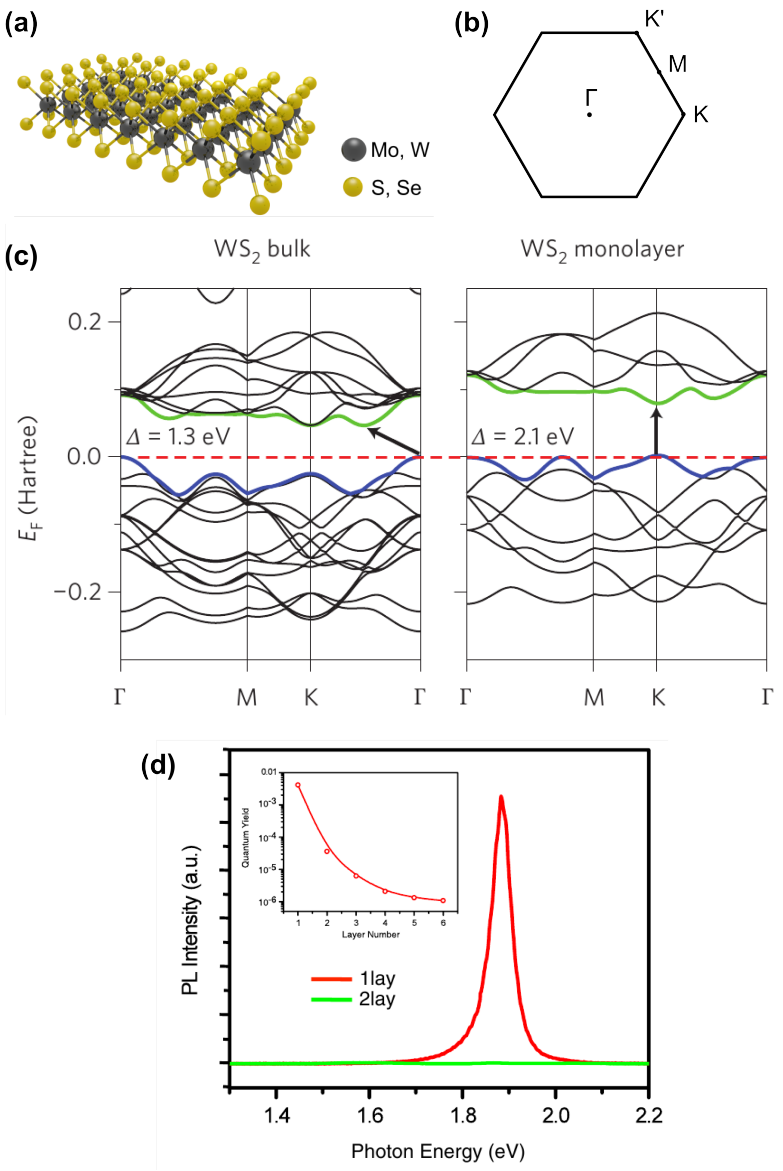


Figure 1.1: **Transition metal dichalcogenides.** (a) Illustration of a TMD monolayer. (b) Symmetry points of the reciprocal lattice (momentum space). (c) Band structure of bluk and monolayer $WS_2$. While the bulk material has an indirect bandgap, the monolayer has a direct bandgap at the K point. Figure taken from [7]. (d) Spectrally-resolved photoluminescence as a function of number of layers. The photoluminescence of monolayers is stronger than in bulk materials and is centered at the exciton resonance energy. Figure taken from [9].

# Chapter 2

# Theoretical basis

## 2.1 Density matrix formalism in second quantization

### 2.1.1 Second quantization

In order to efficiently treat a many-particle system, it is useful to describe it in second quantization. To this end, the creation and annihilation operators $a_i^\dagger$ and $a_i$ acting on the state $i$ are introduced, which fulfill the following commutation relations:

$$\left[a_i, a_j\right]_\pm = \left[a_i^\dagger, a_j^\dagger\right]_\pm = 0 \tag{2.1}$$

$$\left[a_i^\dagger, a_j\right]_\pm = \delta_{ij} \tag{2.2}$$

Fermions fulfill the anticommutation relations $(+)$, while bosons fulfill the commutation relations $(-)$. Any one- or two-particle operator can be expressed in terms of these operators:

$$\hat{O}^{(1)} = \sum_{ij} O_{ij} a_i^\dagger a_j \tag{2.3}$$

$$\hat{O}^{(2)} = \sum_{ijlm} O_{lm}^{ij} a_i^\dagger a_j^\dagger a_l \, a_m \tag{2.4}$$

with the matrix elements of the operator $\hat{O}$ being:

$$O_{ij} = \left\langle i \middle| \hat{O}^{(1)} \middle| j \right\rangle = \int_{\mathbb{R}^3} d^3\mathbf{r} \; \phi_i^*(\mathbf{r}) \; \hat{O}^{(1)}(\mathbf{r}) \; \phi_j(\mathbf{r}) \tag{2.5}$$

$$O_{lm}^{ij} = \left\langle i, j \middle| \hat{O}^{(2)} \middle| l, m \right\rangle = \int_{\mathbb{R}^3} d^3\mathbf{r} d^3\mathbf{r}' \phi_i^*(\mathbf{r}) \; \phi_j^*(\mathbf{r}') \; \hat{O}^{(2)}(\mathbf{r}, \mathbf{r}') \; \phi_l(\mathbf{r}') \; \phi_m(\mathbf{r}) \tag{2.6}$$

This relation can be applied to the Hamiltonian of the system for a simple and interpretable picture. At the same time, the creation and annihilation operators can be used to define microscopic quantities such as carrier occupation and phonon number. These quantities will be presented in section 2.2.1.

### 2.1.2 Heisenberg equation of motion

The time evolution of the mentioned microscopic quantities is described by Heisenberg's equation of motion. As the Schrödinger equation describes the time evolution of wavefunctions (Schrödinger's picture), this analogous equation describes the time evolution of quantum-mechanical operators (Heisenberg's picture). In our case, it is useful to find expressions for the dynamics of some density matrix $\rho_{ij} = \langle a_i^\dagger a_j \rangle$:

$$i\hbar \frac{d\rho_{ij}}{dt} = \left\langle \left[ a_i^\dagger a_j, \hat{H} \right]_- \right\rangle \tag{2.7}$$

where $\hbar$ is the reduced Planck constant and $\hat{H}$ is the Hamiltonian of the system. From now on, any time derivative will be expressed with a dot, i.e. $\dot{\rho}_{ij}$.

### 2.1.3 Correlation expansion

A direct consequence of applying Heisenberg's equation in a system with many-particle interaction is the hierarchy problem. When calculating the commutator (2.7), another unknown microscopic quantity of higher order will appear, which will need its own equation of motion. The same problem will appear for this new quantity, thus yielding a system of equations which is not closed. In order to solve this problem a correlation expansion can be used up to some order at which the expansion is truncated. An illustrative example of the correlation expansion is the Hartree-Fock approximation:

$$\langle a_i^\dagger a_j^\dagger a_k a_l \rangle = \langle a_i^\dagger a_l \rangle \langle a_j^\dagger a_k \rangle - \langle a_i^\dagger a_k \rangle \langle a_j^\dagger a_l \rangle + \langle a_i^\dagger a_j^\dagger a_k a_l \rangle^c \tag{2.8}$$

where $\langle a_i^\dagger a_j^\dagger a_k a_l \rangle^c = 0$ gives the truncation to two-operator quantities. This equation will be used to calculate the contribution of carrier-carrier interaction to the equations of motion.

### 2.1.4 Markov approximation

During the derivation of the scattering contributions to the equations of motion, intermediate equations of the following form will be encountered:

$$\dot{x}(t) = (i\omega - \gamma)x(t) + iQ(t) \tag{2.9}$$

Assuming $x(t_0) = 0$, a solution to this equation is

$$x(t) = i \int_0^\infty dt' e^{(i\omega-\gamma)t'} Q(t-t') \tag{2.10}$$

As in other contexts, here the Markov approximation consists in neglecting memory effects. This can be justified when the quantity $Q(t-t')$ varies slowly with respect to the oscillation $e^{i\omega_Q t'}$. This approximation leads to a simple and intuitive solution:

$$x(t) = i\pi Q(t)\delta(\omega - \omega_Q) \tag{2.11}$$

where $\gamma \to 0$ has been assumed. The limit of a vanishing damping ($\gamma$) yields to a strict energy conservation (fulfilled inside the delta function). This situation corresponds to suppressing fluctuations arising from Heisenberg's uncertainty principle.

## 2.2 Equations of motion

### 2.2.1 Microscopic quantities

As previously mentioned, the creation and annihilation operators can be used to build density matrices that describe microscopic quantities which, for instance, can correspond to particle or quasi-particle densities. In a semiconductor, and more concretely in the kind of systems that are studied in this thesis, the quantities of interest are the electron occupation $\rho^l_{\mathbf{k}}$, phonon number $n^j_{\mathbf{q}}$, photon number $n^{\mathrm{pt}}_{\mathbf{q}}$, and microscopic polarization $p_{\mathbf{k}}$. The first three correspond to quantum particles or quasi-particles, with the electron being a fermion with negative elementary charge, a phonon being a quantum of lattice vibration, and a photon being a quantum of the electromagnetic field. The microscopic polarization describes the coherence between states in the valence and the conduction band generated by an optical excitation. The relations between these quantities and the creation and annihilation operators are:

$$\rho^l_{\mathbf{k}} = \left\langle a^{l\dagger}_{\mathbf{k}} a^l_{\mathbf{k}} \right\rangle \tag{2.12}$$

$$n^j_{\mathbf{q}} = \left\langle b^{j\dagger}_{\mathbf{q}} b^j_{\mathbf{q}} \right\rangle \tag{2.13}$$

$$n^{\mathrm{pt}}_{\mathbf{q}} = \left\langle c^{\mathrm{pt}\dagger}_{\mathbf{q}} c^{\mathrm{pt}}_{\mathbf{q}} \right\rangle \tag{2.14}$$

$$p_{\mathbf{k}} = \left\langle a^{c\dagger}_{\mathbf{k}} a^v_{\mathbf{k}} \right\rangle \tag{2.15}$$

where $l = c, v$ is the electronic band, $j$ is the phonon mode, and $\mathbf{k}$ and $\mathbf{q}$ are two-dimensinoal momentum vectors.

It is also useful to introduce hole occupation in the valence band. In this way, we will deal with quasi-particles that are analogous to electrons in the conduction

band. Electrons in the conduction band and holes in the valence band are commonly called charge-carriers, because they transport charge along the material and are able to generate electrical currents. From now one $\rho^l_{\mathbf{k}}$ will be replaced by $f^\lambda_{\mathbf{k}}$, with $f^e_{\mathbf{k}} = \rho^c_{\mathbf{k}}$ and $f^h_{\mathbf{k}} = 1 - \rho^v_{\mathbf{k}}$.

### 2.2.2 Hamiltonian of the system

In order to derive equations of motion for the microscopic quantities introduced above, we need to find the system's Hamiltonian. The phenomena that are studied in this thesis usually consist of (1) optical excitation, (2) carrier relaxation, and (3) carrier-carrier interaction. According to the Bohr-Oppenheimer approximation, electrons can be decoupled from the lattice (phonons), so that carrier-carrier, carrier-phonon and phonon-phonon interactions can be described intependently. The different contributions to the Hamiltonian are introduced below.

#### Free particle

Carriers in a semiconductor have a given band structure that arises from their zero-order interaction with the lattice. Analogously, phonons also have a given energy-dispersion. This can be introduced in the Hamiltonian as a one-particle operator:

$$H_0 = \sum_i \varepsilon_i a_i^\dagger a_i + \sum_j \hbar\Omega_j b_j^\dagger b_j \tag{2.16}$$

where $i = \lambda, \mathbf{k}$ and $j = j, \mathbf{q}$ correspond to the carrier and phonon states, respectively. Note that spin is neglected in this thesis as no magnetic fields are considered.

In real semiconductors, the electronic and phononic band structures have several branches with complicated momentum-dependences. While these can be calculated using density functional theory, their implementation in our equations would be numerically demanding. However, the dynamics of our interest take place at the minima of the energy bands. In the electronic band-structure, the energy dispersion can be approximated around these so-called symmetry points (see figure 1.1b) as the one of free electrons with an effective mass, i.e. $\varepsilon^\lambda_{\mathbf{k}} = \frac{1}{2}\varepsilon_g + \hbar^2\mathbf{k}^2(2m_\lambda)^{-1}$. Analogously, the phonon energy-dispersions can be approximated for small momenta using the Debye and Einstein approaches for acoustic and optical phonons, respectively. In these approaches, acoustic phonons have a linear energy dispersion with constant velocity, while optical phonons have a constant energy dispersion.

### Carrier-light interaction

In order to describe the optical excitation of carriers, it is sufficient to consider light as a classical electromagnetic field rather than in a quantum-mechanical description. Under this semiclassical approach, this contribution to the Hamiltonian can be written in terms of the vector potential $\mathbf{A}(t)$ and the optical matrix element $\mathbf{M}_{ij} = \langle i|\nabla|j\rangle$:

$$H_{c-l} = i\hbar\frac{e_0}{m_0}\sum_{ij}\mathbf{M}_{ij}\cdot\mathbf{A}(t)a_i^\dagger a_j \tag{2.17}$$

where $e_0$ and $m_0$ are the elementary charge and the free electron mass, respectively. In general, only interband direct transitions are allowed under optical irradiation. In this case, the carrier-light Hamiltonian illustrates the excitation of an electron from the valence to the conduction band by an external optical source.

### Carrier-phonon interaction

The carrier-phonon Hamiltonian illustrates all possible electronic transitions assisted by the absorption or emission of a phonon.:

$$H_{c-p} = \sum_{ijl}\left(g_{ij}^l a_i^\dagger a_j b_l + g_{ij}^{l*} a_j^\dagger a_i b_l^\dagger\right) \tag{2.18}$$

where the electron-phonon coupling element

$$g_{ij}^l = \sqrt{\frac{\hbar}{2M\Omega_l}}\langle i|\Delta V_l|j\rangle \tag{2.19}$$

has been introduced. Here $M$ is the mass of the unit cell and $\Delta V_l$ is the *scattering potential* and can be approximated in zero and first order by the deformation potential approximation [14].

### Carrier-carrier interaction

The carrier-carrier Hamiltonian describes a two-particle interaction between two electrons through Coulomb interaction:

$$H_{c-c} = \frac{1}{2}\sum_{ijlm}V_{lm}^{ij}a_i^\dagger a_j^\dagger a_l a_m \tag{2.20}$$

where $V_{lm}^{ij} = \langle i,j|V(\mathbf{r}'-\mathbf{r})|l,m\rangle$ is the Coulomb matrix element, with $V(\mathbf{r}'-\mathbf{r})$ being the Coulomb potential. At small momenta and considering only intraband transitions the Coulomb matrix element corresponds to the Coulomb potential in

momentum space, $V_{\mathbf{q}}$. In order to better describe TMDs, which are not completely two-dimensional (the height of the layer is about 0.6 nm), the Rytova-Keldysh potential is used [22–24].

The Hamiltonian of this system is thus the sum of the previous contributions:

$$H = H_0 + H_{c-l} + H_{c-p} + H_{c-c} \tag{2.21}$$

### 2.2.3 Momentum-resolved equations of motion

Inserting the Hamiltonian of the system into Heisenberg's equation of motion allows us to find expressions for the time evolution of the quantities of our interest, i.e. polarization, carrier occupation, and phonon number:

$$\dot{p}_{\mathbf{k}} = i\left(\Delta\tilde{\omega}_{\mathbf{k}} + i\gamma_{\mathbf{k}}\right)p_{\mathbf{k}} - \left(1 - f^e_{\mathbf{k}} - f^h_{\mathbf{k}}\right)\tilde{\Omega}_{\mathbf{k}} \tag{2.22}$$

$$\dot{f}^{\lambda}_{\mathbf{k}} = 2\Im\left\{\tilde{\Omega}^*_{\mathbf{k}}p_{\mathbf{k}}\right\} + \Gamma^{\lambda,\text{in}}_{\mathbf{k}}\left(1 - f^{\lambda}_{\mathbf{k}}\right) - \Gamma^{\lambda,\text{out}}_{\mathbf{k}}f^{\lambda}_{\mathbf{k}} \tag{2.23}$$

$$\dot{n}^j_{\mathbf{q}} = \Gamma^{j,\text{em}}_{\mathbf{q}}\left(1 + n^j_{\mathbf{q}}\right) - \Gamma^{j,\text{abs}}_{\mathbf{q}}n^j_{\mathbf{q}} - \kappa^j n^j_{\mathbf{q}} \tag{2.24}$$

where carrier-carrier scattering and carrier-recombination have been neglected. There are different terms in these equations that account for different phenomena.

The oscillation frequency $\hbar\Delta\omega_{\mathbf{k}} = \varepsilon^e_{\mathbf{k}} + \varepsilon^h_{\mathbf{k}}$ is renormalized due to many-particle Coulomb interaction:

$$\hbar\Delta\tilde{\omega}_{\mathbf{k}} = \tilde{\varepsilon}_{\mathbf{k}} = \hbar\Delta\omega_{\mathbf{k}} + \sum_{\mathbf{k}'} W_{|\mathbf{k}-\mathbf{k}'|}\left(1 - f^e_{\mathbf{k}} - f^h_{\mathbf{k}}\right) \tag{2.25}$$

where $W_{|\mathbf{k}-\mathbf{k}'|}$ is the screened potential, with the screening being computed according to the static Lindhard formula:

$$W_{|\mathbf{k}-\mathbf{k}'|} = \frac{V_{|\mathbf{k}-\mathbf{k}'|}}{\epsilon_{|\mathbf{k}-\mathbf{k}'|}}, \quad \epsilon_{\mathbf{q}} = 1 - V_{\mathbf{q}}\sum_{\lambda\mathbf{k}}\frac{f^{\lambda}_{\mathbf{k}-\mathbf{q}} - f^{\lambda}_{\mathbf{k}}}{\varepsilon^{\lambda}_{\mathbf{k}-\mathbf{q}} - \varepsilon^{\lambda}_{\mathbf{k}}} \tag{2.26}$$

The screening contribution to the equations of motion can be derived by taking into account higher order terms in the correlation expansion [25]. Since the energy bandgap at zero carrier density is provided already taking into account many-particle unscreened Coulomb interaction, it is more correct to write equation 2.25 as:

$$\hbar\Delta\tilde{\omega}_{\mathbf{k}} = \varepsilon^e_{\mathbf{k}} + \varepsilon^h_{\mathbf{k}} + \sum_{\mathbf{k}'}\left(W_{|\mathbf{k}-\mathbf{k}'|} - V_{|\mathbf{k}-\mathbf{k}'|}\right) - \sum_{\mathbf{k}'}W_{|\mathbf{k}-\mathbf{k}'|}\left(f^e_{\mathbf{k}} + f^h_{\mathbf{k}}\right) \tag{2.27}$$

where the second and third terms correspond to the Coulomb-hole and screened exchange interactions, respectively [11].

Analogously, the Rabi frequency $\Omega_0$ is also renormalized due to many-particle Coulomb interaction:

$$\tilde{\Omega}_{\mathbf{k}} = \Omega_0 - \sum_{\mathbf{k}'} W_{|\mathbf{k}-\mathbf{k}'|} p_{\mathbf{k}'} \tag{2.28}$$

The Rabi frequency, $\Omega_0 = i\frac{e_0}{m_0}\mathbf{M}^{vc} \cdot \mathbf{A}(t)$, is the driving term and accounts for the optical excitation. The Coulomb-induced renormalization (second term in the equation above) accounts for excitonic effects in the Hartree-Fock level. It is important to note the phase-space filling factor, $1 - f^e_{\mathbf{k}} - f^h_{\mathbf{k}}$, that appears in front of the Rabi frequency and is a direct manifestation of fermionic Pauli-blocking. When there is the same number of electrons at the same momentum-state in the conduction and valence band ($f^e_{\mathbf{k}} = 1 - f^h_{\mathbf{k}}$), optical transitions are blocked and hence this term is zero. Thus, this term modulates the strength and sign of the generation of microscopic polarization. At very high carrier densities, this term changes sign, describing optical gain caused by population inversion.

The carrier-phonon scattering rates $\Gamma$ arise from the second order Born-Markov approximation and resemble Fermi's golden rule for the scattering transitions:

$$\Gamma^{\lambda,\text{in}}_{\mathbf{k}} = \frac{2\pi}{\hbar}\sum_{j\mathbf{q}\pm} \left|g^{\lambda j}_{\mathbf{q}}\right|^2 f^{\lambda}_{\mathbf{k}+\mathbf{q}} \left(\frac{1}{2} \pm \frac{1}{2} + n^j_{\pm\mathbf{q}}\right) \delta\left(\varepsilon^{\lambda}_{\mathbf{k}} - \varepsilon^{\lambda}_{\mathbf{k}+\mathbf{q}} \pm \hbar\Omega^j_{\mathbf{q}}\right) \tag{2.29}$$

$$\Gamma^{\lambda,\text{out}}_{\mathbf{k}} = \frac{2\pi}{\hbar}\sum_{j\mathbf{q}\pm} \left|g^{\lambda j}_{\mathbf{q}}\right|^2 \left(1 - f^{\lambda}_{\mathbf{k}-\mathbf{q}}\right) \left(\frac{1}{2} \pm \frac{1}{2} + n^j_{\pm\mathbf{q}}\right) \delta\left(\varepsilon^{\lambda}_{\mathbf{k}-\mathbf{q}} - \varepsilon^{\lambda}_{\mathbf{k}} \pm \hbar\Omega^j_{\mathbf{q}}\right) \tag{2.30}$$

$$\Gamma^{j,\text{em}}_{\mathbf{k}} = \frac{2\pi}{\hbar}\sum_{\lambda\mathbf{k}} \left|g^{\lambda j}_{\mathbf{q}}\right|^2 f^{\lambda}_{\mathbf{k}} \left(1 - f^{\lambda}_{\mathbf{k}-\mathbf{q}}\right) \delta\left(\varepsilon^{\lambda}_{\mathbf{k}} - \varepsilon^{\lambda}_{\mathbf{k}-\mathbf{q}} - \hbar\Omega^j_{\mathbf{q}}\right) \tag{2.31}$$

$$\Gamma^{j,\text{abs}}_{\mathbf{k}} = \frac{2\pi}{\hbar}\sum_{\lambda\mathbf{k}} \left|g^{\lambda j}_{\mathbf{q}}\right|^2 f^{\lambda}_{\mathbf{k}} \left(1 - f^{\lambda}_{\mathbf{k}+\mathbf{q}}\right) \delta\left(\varepsilon^{\lambda}_{\mathbf{k}} - \varepsilon^{\lambda}_{\mathbf{k}+\mathbf{q}} + \hbar\Omega^j_{\mathbf{q}}\right) \tag{2.32}$$

These terms lead the excited distributions to an equilibrium (Fermi-Dirac distribution for carriers and Bose-Einstein distribution for phonons). The dephasing of the microscopic polarization corresponds to the loss of coherence caused by scattering with phonons:

$$\gamma_{\mathbf{k}} = \frac{1}{2}\sum_{\lambda} \left(\Gamma^{\lambda,\text{in}}_{\mathbf{k}} + \Gamma^{\lambda,\text{out}}_{\mathbf{k}}\right) \tag{2.33}$$

Scattering with phonons would also introduce an off-diagonal dephasing which is negligible.

Finally, a phenomenological phonon decay $\kappa^j$ is introduced. In a more complete model, this term could be derived from phonon-phonon scattering, which is not considered here due to its complexity.

For illustrative purposes, the system of equations presended here is numerically solved in the simple case of a weak excitation, where many-particle dielectric

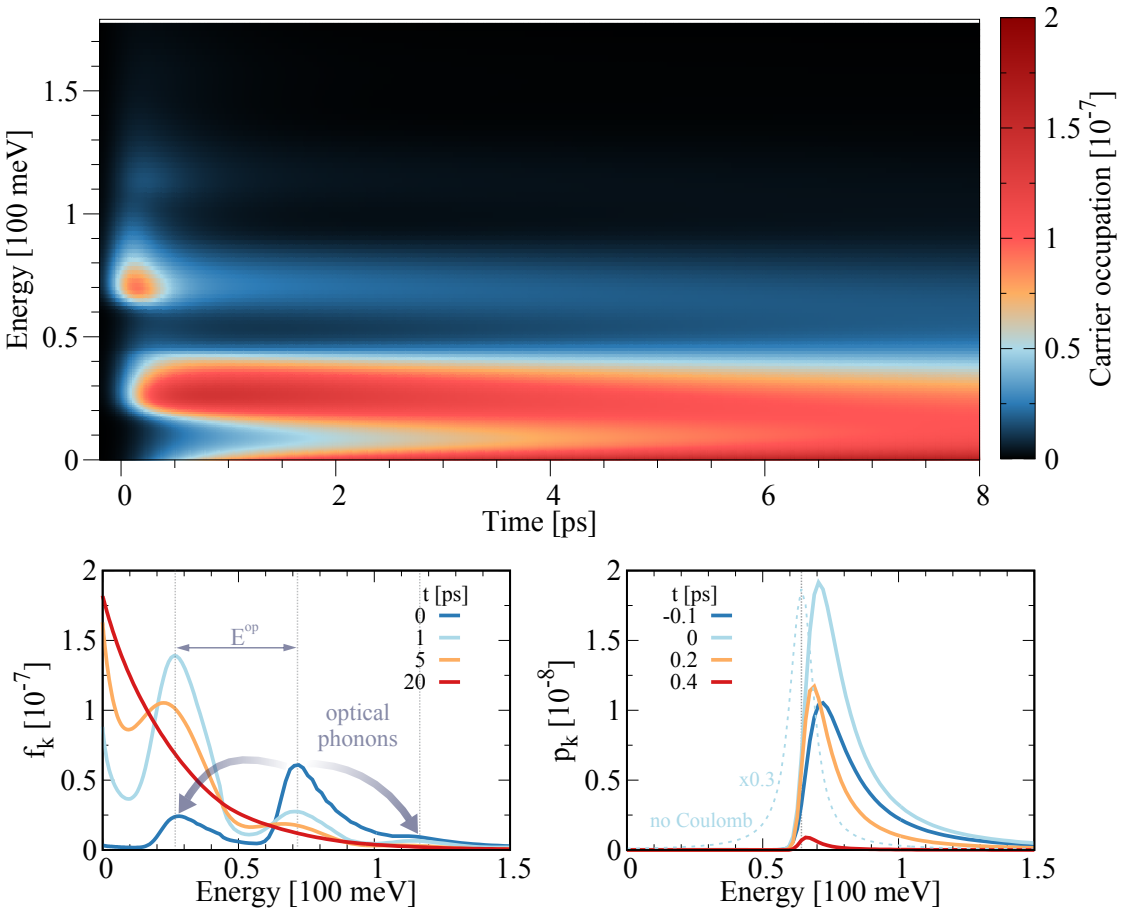


Figure 2.1: **Carrier excitation and relaxation.** Energy-resolved time evolution of carrier occupation (colormap and bottom left figure) and microscopic polarization (bottom right). The arrows in the bottom left plot illustrate scattering of carriers with optical phonons. The dashed lines in the bottom right plot show the excitation energy and the microscopic polarization calculated without the effect of Coulomb interaction.

screening, energy renormalization, bleaching effects and hot-phonon effects are negligible. As shown in Figure 2.1, microscopic polarization with finite energy is generated by an optical excitation with an energy higher than the bandgap of the material. This microscopic polarization (also called coherence) is the responsible for exciting carriers with the energy given by the pulse. Due to phonon-induced dephasing, the coherence quickly decays a few tens of femtoseconds (1 fs is $10^{15}$ s) after the optical excitation. The excited carriers first undergo scattering with optical phonons in a timescale of hundreds of femtoseconds. Due to the constant energy dispersion of optical phonons, the result of scattering with optical phonons

is the replication of the excited carrier peak with an energy difference given by the optical phonon energy, as illustrated by the arrows in the figure. When most carriers have scattered to energies lower than the optical phonon energy, relaxation by scattering with optical phonons is no longer possible. Then, the main relaxation channel is scattering with accoustic phonons, which slowly leads the carriers into an equilibrium Fermi distribution in a timescale of tens of picoseconds.

The effect of Coulomb interaction in the microscopic polarization is also illustrated in the figure, showing that it shifts the resonance energy of the microscopic polarization and alters its shape in energy. Nevertheless, the elongated tail of the microscopic polarization into higher energies might in fact be an artifact that arises from neglecting Coulomb effects when deriving the phonon-induced dephasing.

### 2.2.4 Space- and momentum-resolved equations of motion

The equations presented above only describe the time evolution of the system in momentum space. It is interesting, however, to extend these equations to real space in order to study spatio-temporal phenomena such as diffusion or electric transport. To this end it is convenient to introduce Wigner functions [26]:

$$f_{\mathbf{k}}(\mathbf{r},t) = \sum_{\mathbf{q}} e^{i\mathbf{q}\cdot\mathbf{r}} f_{\mathbf{k}-\frac{1}{2}\mathbf{q},\mathbf{k}+\frac{1}{2}\mathbf{q}} \tag{2.34}$$

where $f_{\mathbf{k}_1,\mathbf{k}_2} = \left\langle a^\dagger_{\mathbf{k}_1} a_{\mathbf{k}_2} \right\rangle$ is a one-particle off-diagonal density matrix. While diagonal one-particle density matrices can be interpreted as probability distributions, this interpretation is not appropiate for Wigner functions since they can be negative. This non-intuitive property of Wigner functions arises naturally from the uncertainty principle in quantum mechanics. In this sense, Wigner functions are defined as quasi-probability distributions. When integrating over momentum or real space, the probability distribution in each respective space is obtained:

$$n(\mathbf{r}) = \sum_{\mathbf{k}} f_{\mathbf{k}}(\mathbf{r}), \quad n(\mathbf{k}) = \sum_{\mathbf{r}} f_{\mathbf{k}}(\mathbf{r}) \tag{2.35}$$

Having introduced the Wigner formalism, it is straightforward to find general expressions for the space- and momentum-resolved equations of motion. The procedure consists in first deriving equations of motion for the off-diagonal density matrices $f_{\mathbf{k}_1,\mathbf{k}_2}$ and then multipliying the equations by $e^{i\mathbf{q}\cdot\mathbf{r}}$ and integrating over $\mathbf{q}$. In order to simplify the complicated integro-differential equations that are obtained, a Taylor expansion can be performed up to first order, which is sufficient to describe the main spatial phenomena [27, 28]. Moreover, any transport terms of the polarization can be neglected since they will happen in a timescale longer than its decay. In addition, the phonon diffusion can in general be neglected because it

is much slower than electron diffusion, and electron-phonon scattering is considered to be local in space because scattering involving particles spatially separated is weak. Thus, the only quantity that has significant terms arising from spatial inhomogeneities is the carrier density. In addition to the local terms (eq. 2.23), two new contributions appear in the equation of motion:

$$\dot{f}^{\lambda}_{\mathbf{k}}(\mathbf{r},t)\Big|_{\text{space}} = -\mathbf{v}^{\lambda}_{\mathbf{k}} \cdot \nabla_{\mathbf{r}} f^{\lambda}_{\mathbf{k}}(\mathbf{r},t) + \frac{e_0}{\hbar}\nabla_{\mathbf{r}}\tilde{\Phi}^{\lambda}_{\mathbf{k}}(\mathbf{r},t)\nabla_{\mathbf{k}} f^{\lambda}_{\mathbf{k}}(\mathbf{r},t) \tag{2.36}$$

The first term describes the movement of carriers with velocity $\mathbf{v}^{\lambda}_{\mathbf{k}} = \pm\nabla_{\mathbf{k}}\tilde{\omega}^{\lambda}_{\mathbf{k}}(\mathbf{r},t)$, where $\pm$ corresponds to electrons and holes respectively. Note that the velocity of the carriers can be space- and time-dependent due to density-dependent band renormalization. The spatial gradient of the carrier occupation accounts for the difference between the out-going and in-coming particles.

The second term describes the acceleration of carriers in momentum space caused by a potential gradient, which can be an electric field or the spatial energy gradient caused by inhomogeneous energy renormalization. The generalized potential gradient has the form $\nabla_{\mathbf{r}}\tilde{\Phi}^{\lambda}_{\mathbf{k}} = -\mathbf{E}^{\text{ext}} - \mathbf{E}^{\text{int}} \pm \frac{\hbar}{e_0}\nabla_{\mathbf{r}}\tilde{\omega}^{\lambda}_{\mathbf{k}}$, with externally applied and internally induced electric fields $\mathbf{E}^{\text{ext}}$ and $\mathbf{E}^{\text{int}}$, and the renormalized band structure $\hbar\tilde{\omega}^{\lambda}_{\mathbf{k}}$. The internal electric field is induced by the local net charge that is created due to the difference in electron and hole occupation. This inhomogeneous difference can be obtained by doping (e.g. in a pn junction) or under optical excitation by the simple fact that electrons propagate faster than holes. The internal electric field can be obtained from the following expression:

$$\mathbf{E}^{\text{int}} = -\nabla_{\mathbf{r}} \int_{\mathbb{R}^2} d^2\mathbf{r}'\; W(\mathbf{r}-\mathbf{r}') \left[n^h(\mathbf{r}') - n^e(\mathbf{r}')\right] \tag{2.37}$$

A more thorough derivation and discussion of these expressions can be found in [27, 28].

## 2.3 Excitons

### 2.3.1 Excitonic basis and Wannier equation

The equation of motion for the microscopic polarization (2.22) can be solved by expanding $p_{\mathbf{k}}$ in an orthonormal basis of wavefunctions [13]:

$$p_{\mathbf{k}} = \sum_{\nu} p^{\nu} \phi_{\mathbf{k}}^{\nu R} \tag{2.38}$$

$$p^{\nu} = \sum_{\mathbf{k}} \phi_{\mathbf{k}}^{\nu L *} p_{\mathbf{k}} \tag{2.39}$$

$$\sum_{\mathbf{k}} \phi_{\mathbf{k}}^{\nu L *} \phi_{\mathbf{k}}^{\mu R} = \delta_{\nu\mu} \tag{2.40}$$

where $p^{\nu}$ is the polarization of the excitonic state $\nu$, and $\phi_{\mathbf{k}}^{\nu R(L)}$ is the right (left) wavefunction that fulfills the Wannier equation:

$$\tilde{\varepsilon}_{\mathbf{k}} \phi_{\mathbf{k}}^{\nu R} - \left(1 - f_{\mathbf{k}}^{e} - f_{\mathbf{k}}^{h}\right) \sum_{\mathbf{k}'} W_{|\mathbf{k}-\mathbf{k}'|} \phi_{\mathbf{k}'}^{\nu R} = \varepsilon^{\nu} \phi_{\mathbf{k}}^{\nu R} \tag{2.41}$$

$$\phi_{\mathbf{k}}^{\nu L *} \tilde{\varepsilon}_{\mathbf{k}} - \sum_{\mathbf{k}'} \phi_{\mathbf{k}'}^{\nu L *} \left(1 - f_{\mathbf{k}'}^{e} - f_{\mathbf{k}'}^{h}\right) W_{|\mathbf{k}-\mathbf{k}'|} = \phi_{\mathbf{k}}^{\nu L *} \varepsilon^{\nu} \tag{2.42}$$

The use of left and right eigenfunctions is necessary when the matrix of the eigenproblem is not Hermitian. This can be the case when the carrier occupations $f_{\mathbf{k}}^{e(h)}$ are non-zero. In addition to the excitonic wavefunctions, the Wannier equation provides access to the excitonic resonance energies $\varepsilon^{\nu}$. From the symmetry of the Wannier equation, a relation between the left and right wavefunctions can be found:

$$\phi_{\mathbf{k}}^{\nu R} = \left(1 - f_{\mathbf{k}}^{e} - f_{\mathbf{k}}^{h}\right) \phi_{\mathbf{k}}^{\nu L} \tag{2.43}$$

This relation holds as long as $1 - f_{\mathbf{k}}^{e} - f_{\mathbf{k}}^{h} \neq 0$.

It is noteworthy to mention the phase-space filling factor in the Wannier equation, which modulates the strength and sign of the Coulomb potential. While at low carrier densities the Coulomb potential is attractive, at population inversion it is repulsive and there are no bound excitonic states. The transition from the bound-exciton regime at low densities to the electron-hole plasma regime at high densities is called excitonic Mott transition.

The Wannier equation is easily solvable in the simple case when the carrier densities are zero. Figure 2.2 shows the wavefunctions of the first three excitonic states of *s*-type, which are isotropic. Excitonic states with higher symmetry (p, d, f, etc.) do not contribute significantly to the optical response of TMDs in

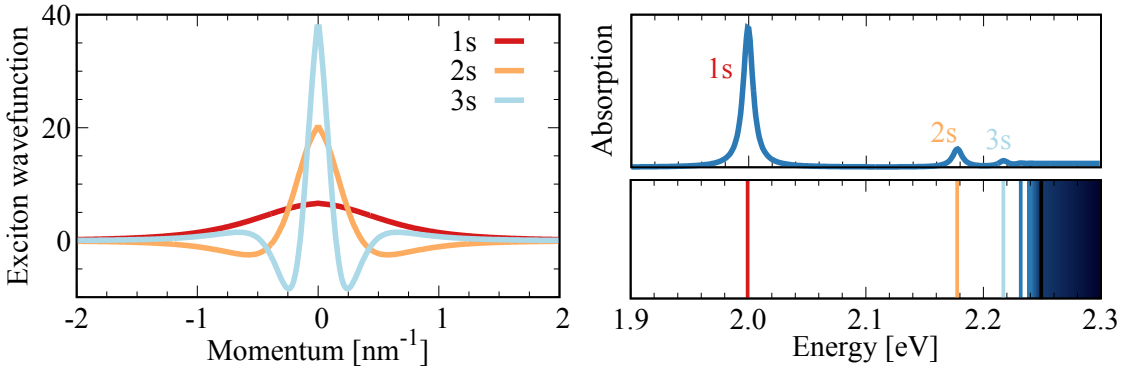


Figure 2.2: **Excitons properties.** Left: excitonic wavefunctions at zero carrier density as a function of momentum. Right: exciton resonance energies (bottom) and optical absorption (top). The black line in the bottom plot marks the position of the bandgap.

the studied regimes and are therefore not shown here. The calculated exciton wavefunctions have a number of nodes corresponding to their quantum number (0 nodes for the 1s, 1 node for the 2s, 2 nodes for the 3s, and so on). By solving the Wannier equation one also obtain the exciton energies. As shown in the figure, the three exciton states shown are clearly below the bandgap (which is chosen to be 2.25 eV), with the 1s binding energy being over 200 meV. This implies that even at room temperature – thermal fluctiation of 25 meV – these are bound states and dominate the characteristics of the system. Optical absorption, which is also shown, will be discussed in the next section.

### 2.3.2 Optical absorption spectra – Elliot formula

A direct use of the excitonic wavefunctions and binding energies is to find the optical absorption spectra of a given material. The optical absorption in the weak excitation regime holds:

$$\alpha(\omega) \propto \Im\{\chi(\omega)\} = \frac{P(\omega)}{\epsilon_0 E(\omega)} = \frac{j(\omega)}{\epsilon_0 \omega^2 A(\omega)} \tag{2.44}$$

where $\chi$ is the electric susceptibility, $P$ the macroscopic polarization, $E$ the electric field, $j$ the current density, and $A$ the vector potential of the optical excitation. The current density holds:

$$\mathbf{j} \propto \sum_{\mathbf{k}} \Re\{\mathbf{M}_{\mathbf{k}}^{vc*} p_{\mathbf{k}}\} \tag{2.45}$$

Thus, by combining equations 2.22, 2.38, 2.39, 2.41, 2.42, 2.44 and 2.45 an expression for the optical absorption spectra can be found:

$$\alpha(\omega) \propto \frac{|M_\sigma^{vc}|^2}{\omega} \sum_\nu \Im \left\{ \frac{\sum_{\mathbf{k}} \left(1 - f_{\mathbf{k}}^e - f_{\mathbf{k}}^h\right) \phi_{\mathbf{k}}^{\nu L *} \sum_{\mathbf{k}} \phi_{\mathbf{k}}^{\nu R}}{\hbar\omega - \varepsilon^\nu + i\gamma} \right\} \tag{2.46}$$

where $M_\sigma^{vc}$ is the dot product between the light polarization and the optical matrix element, and a constant dephasing $\gamma$ has been assumed for the sake of simplicity. As long as there is no population inversion ($f_{\mathbf{k}}^e + f_{\mathbf{k}}^h \neq 0$), the expression above can be simplified to:

$$\alpha(\omega) \propto \frac{|M_\sigma^{vc}|^2}{\omega} \sum_\nu \left|\phi^{\nu R}(\mathbf{r}=0)\right|^2 \mathcal{L}_\gamma(\hbar\omega - \varepsilon^\nu) \tag{2.47}$$

where $\phi^{\nu R}(\mathbf{r}) = \sum_{\mathbf{k}} e^{i\mathbf{k}\cdot\mathbf{r}} \phi_{\mathbf{k}}^{\nu R}$ has been used. This expression can be understood as the sum over all excitonic states $\nu$, each one having an optical absorption with an oscillator strength given by the probability of an electron and a hole being at the same position and a shape described by a Lorentzian $\mathcal{L}$ centered at the excitonic resonance energy $\varepsilon^\nu$ with a broadening $\gamma$. More information regarding exciton wavefunctions and optical absorption at finite carrier densities can be found in [11–13].

In Figure 2.2, the optical absorption is shown in the case of zero carrier density. As previously discussed, the bound excitonic states dominate the characteristics of the system. Thus, the highest absorption peak is determined by the resonance energy of the 1s excitonic state and the corresponding oscillator strength. Higher excitonic states (2s and 3s) also contribute significantly to the optical absorption spectrum, although with a much weaker intensity. As shown in the figure, optical absorption in the excitonic states is enhanced with respect to absorption over the bandgap. Surprisingly, due to the strong Coulomb interaction in these materials carriers can be excited (and in fact their excitation is enhanced) at certain energies lower than the bandgap.

### 2.3.3 Exciton equations of motion

In order to follow the dynamics of excitons, it is useful to define exciton creation and annihilation operators acting on an excitonic state $\nu$ with momentum $\mathbf{Q}$, $X_{\mathbf{Q}}^{\nu\dagger}$ and $X_{\mathbf{Q}}^{\nu}$ respectively, and build an excitonic Hamiltonian [29]. The quantities of interest in this case are the coherent excitonic polarization $P_{\mathbf{Q}}^{\nu}$ and the incoherent

exciton occupation $N^{\nu}_{\mathbf{Q}}$. These quantities are defined as follows:

$$P^{\nu}_{\mathbf{Q}} = \left\langle X^{\nu\dagger}_{\mathbf{Q}} \right\rangle \tag{2.48}$$

$$N^{\nu}_{\mathbf{Q}} = \left\langle X^{\nu\dagger}_{\mathbf{Q}} X^{\nu}_{\mathbf{Q}} \right\rangle - \left| \left\langle X^{\nu\dagger}_{\mathbf{Q}} \right\rangle \right|^2 \tag{2.49}$$

Considering exciton-light and exciton-phonon interactions, the excitonic Hamiltonian can be plugged into Heisenberg's equation to obtain equations of motion for the quantities defined above. As in the case of carriers, when the Wigner representation is considered an additional term appears accounting for spatial propagation. The equations of motion can then be expressed as follows [30]:

$$\dot{P}^{\nu}(\mathbf{r},t) = \frac{i}{\hbar}\left(\varepsilon^{\nu} + i\Gamma^{\nu,\mathrm{rad}} + i\hbar\frac{1}{2}\sum_{\mu\mathbf{Q}}\Gamma^{\nu\mu}_{\mathbf{0Q}}\right)P^{\nu}(\mathbf{r},t) + i\Omega^{\nu}(\mathbf{r},t) \tag{2.50}$$

$$\begin{aligned}\dot{N}^{\nu}_{\mathbf{Q}}(\mathbf{r},t) = &-\mathbf{v}^{\nu}_{\mathbf{Q}}\cdot\nabla_{\mathbf{r}}N^{\nu}_{\mathbf{Q}}(\mathbf{r},t) + \sum_{\mu}\Gamma^{\mu\nu}_{\mathbf{0Q}}\left|P^{\nu}(\mathbf{r},t)\right|^2 - \frac{2}{\hbar}\delta_{\mathbf{Q0}}N^{\nu}_{\mathbf{Q}}(\mathbf{r},t) \\ &+ \sum_{\mu\mathbf{Q}'}\left(\Gamma^{\mu\nu}_{\mathbf{Q}'\mathbf{Q}}N^{\mu}_{\mathbf{Q}'}(\mathbf{r},t) - \Gamma^{\nu\mu}_{\mathbf{QQ}'}N^{\nu}_{\mathbf{Q}}(\mathbf{r},t)\right)\end{aligned} \tag{2.51}$$

Here, $P^{\nu}$ has been defined as the coherent excitonic polarization at zero-momentum, which is the only significant momentum-point since it is the only accessible state by light excitation. We have also introduced the radiative decay rate $\Gamma^{\nu,\mathrm{rad}}$, the scattering matrix $\Gamma^{\nu\mu}_{\mathbf{QQ}'}$, the exciton velocity $\mathbf{v}^{\nu}_{\mathbf{Q}}$ and the Rabi frequency projected into the excitonic state $\nu$ [30–32]:

$$\Gamma^{\nu,\mathrm{rad}} = \frac{\hbar e_0^2}{2m_0^2\epsilon_0 n c_0 \varepsilon^{\nu}}\sum_{\sigma}\left|M^{vc}_{\sigma}\right|^2\left|\sum_{\mathbf{k}}\phi^{\nu}_{\mathbf{k}}\right|^2 \tag{2.52}$$

$$\Gamma^{\nu\mu}_{\mathbf{QQ}'} = \frac{2\pi}{\hbar}\sum_{j\pm}\left|G^{j,\nu\mu}_{\mathbf{Q}-\mathbf{Q}'}\right|^2\left(\frac{1}{2}\pm\frac{1}{2}+n^{j}_{\mathbf{Q}-\mathbf{Q}'}\right)\delta\left(\varepsilon^{\mu}_{\mathbf{Q}'} - \varepsilon^{\nu}_{\mathbf{Q}'} \pm \hbar\Omega^{j}_{\mathbf{Q}-\mathbf{Q}'}\right) \tag{2.53}$$

where $G^{j,\nu\mu}_{\mathbf{Q}-\mathbf{Q}'}$ is the exciton-phonon coupling element and is computed according to the work done by Brem et al. [30].

The equations of motion 2.50 and 2.51 have clear physical meaning. In the equation for the coherent excitonic polarization $P^{\nu}$, the first term corresponds to the polarization oscillation with the frequency given by the exciton energy, the second and third terms represent polarization decay caused by radiative recombination and phonon-induced dephasing, and the fourth term illustrates the creation of coherence by the optical excitation. In the equation for the incoherent exciton occupation, the first term illustrates exciton propagation, the second term accounts for the conversion of coherence into occupation through scattering

with phonons, and the third term corresponds to radiative decay (only possible in the light cone, i.e. at zero-momentum). The last term describes exciton-phonon scattering and results in the thermalization of the excitonic distribution into an equilibrium Boltzmann distribution in momentum-space.

# Chapter 3

# Pump-probe spectroscopy

As presented in the theory of this thesis, it is known that high carrier densities can induce a significant alteration of the exciton properties [10–13]. Consequently, since excitonic effects are dominant in the optical spectra of TMDs, this will result in a significant variation of the optical properties of the material. These effects can be experimentally accessed in ultra-fast pump-probe measurements, where a sample is optically excited by a pump pulse and the induced change in absorption, reflectance or transmittance is measured with the assistance of a probe pulse. Although many pump-probe experiments have been performed for TMDs in the last years [33–38], the conection between the experimental results and the corresponding theoretical explanation is not always clear. In this section, the previously introduced Wannier and semiconductor Bloch equations are combined to calculate the effect of the excited carriers on the exciton properties, as well as their impact on the optical response. Radiative recombination of carriers is introduced here as a phenomenological decay. These studies aim to serve as a tool for understanding the microscopic mechanisms behind experimental observations in pump-probe spectroscopy.

## 3.1 Exciton properties

Solving the semiconductor Bloch equations yields the time evolution of the carriers in energy space (as in Fig. 2.1). Introducing the calculated carrier occupations in the Wannier equation provides the exciton wavefunctions and binding energies at a given time. Thus, the combination of these two equations gives access to the dynamics of exciton properties. At very high excitation conditions, many carriers will be excited, which will translate into high occupation of the electronic states in the minima of the bands. This will have two effects: (1) the phase-space filling factor $(1 - f^e_{\mathbf{k}} - f^h_{\mathbf{k}})$ will be close to zero, thus bleaching the Coulomb interaction

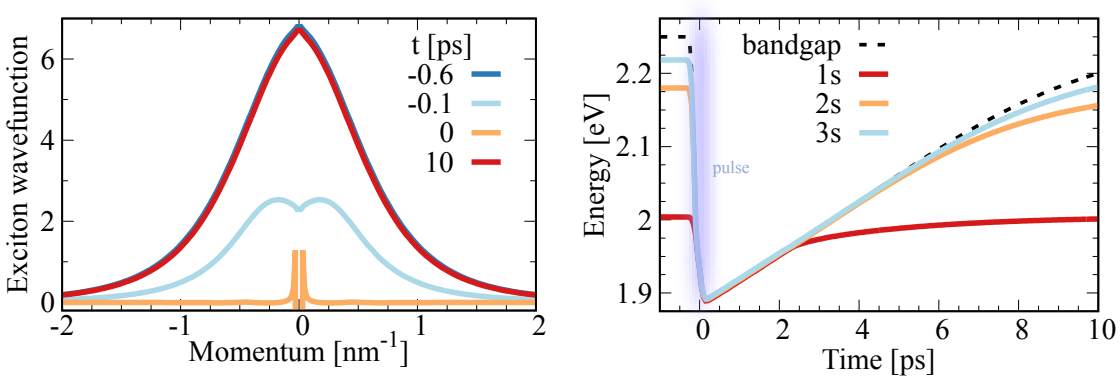


Figure 3.1: **Dynamic change of exciton properties.** Left: bleached excitonic wavefunctions at some times under a 200 fs optical excitation. Right: time evolution of the exciton resonance energies (1s, 2s and 3s) and the bandgap. The purple shaded zone illustrates the pump pulse between -100 and 100 fs.

between electron-hole pairs due to Pauli blocking; and (2) many-particle dielectric screening will significantly reduce the strength of Coulomb interaction.

The dynamics of exciton properties in monolayer $WS_2$ calculated at high excitation with an excitation energy corresponding to the 1s exciton resonance are shown in Figure 3.1. When the pulse starts exciting carriers ($t = -0.1$ ps), the bleaching of the wavefunctions due to Pauli blocking is already noticeable, with the effect being stronger at low momenta because those are the most populated states. At the center of the pulse ($t = 0$ ps) the excitonic wavefunction resembles the one of free states and is negative at very small momentum. While the sign-inversion of the wavefunction at low momenta is directly caused by population inversion, the narrowing in momentum is induced by a combination of many-particle dielectric screening and Pauli blocking. After the pulse excitation, carriers recombine and the population is reduced, resulting in a recovery of the excitonic properties in a timescale given by recombination. This is illustrated by the exciton wavefunction at $t = 10$ ps, which resembles the one before the pulse. Besides the wavefunctions, a high carrier occupation also affects the exciton binding energies and the bandgap. In the figure, it can be seen that the exciton energies and the bandgap remain constant before the optical excitation takes place. Under the strong pulse exciation, the bandgap undergoes a huge red-shift of over 300 meV and the exciton binding energies become smaller – approaching the bandgap and evolving with it – to the point where there are no bound states anymore. After the optical excitation, the bandgap and the exciton resonance energies slowly recover their original values. Note that at sufficiently high carrier densities there are no excitonic bound states and the system is no longer dominated by bound electron-hole pairs but

by an electron-hole plasma. The transition from the insulating excitonic state at low-densities to the metallic electronn-hole plasma at high-density is called Mott transition.

## 3.2 Optical absorption

As introduced in the theory section, the optical absorption of the material can be obtained from the exciton wavefunctions and resonance energies. Hence, the results shown in Figure 3.1 can be used to calculate the temporal evolution of the optical absorption of monolayer $WS_2$ at high excitation. In Figure 3.2, one can see that the excitonic features of the optical absorption are quickly bleached under the strong optical excitation. The excitonic peak undergoes first red-shift and afterwards – apparently – blue-shift. While the first is directly related to the red-shift of the exciton resonance energy, the second is actually not a real shift of the excitonic peak but a bleaching of the optical transition at the lower energetic states caused by the high carrier population. At the same time, the absorption intensity is reduced due to phase-space filling – blocking of the optical transitions – and bleached Coulomb interaction – reduced excitonic enhancement. If the optical excitation is strong enough, it can generate a carrier population inversion – negative phase-space filling factor – which translates into optical gain, i.e. negative absorption. After the optical excitation, the intrinsic optical properties of the material are restored as the carriers recombine and the exciton properties recover their previous values.

In order to experimentally find changes in the absorption spectra, differential absorption – or reflectance, or transmission – spectroscopy is normally used. This technique allows to focus on the changes of the spectra in order to be able to determine even small variations. In practice, it consists in calculating the variation of an optical spectrum at a given time with respect to the spectrum before the excitation of the system. The differential absorption spectra as a function of time calculated from the absorption specta discussed above is also shown in Figure 3.2. In these data, the shift of the absorption peaks can be traced by the zero-cross of the differential absorption, and the bleaching can be identified by a strong negative differential absorption. The huge bandgap renormalization corresponds to the increased absorption between the 1s and 2s exciton energies ($2.0 - 2.2$ eV), and strong carrier occupation and population inversion is responsible for the decreased absorption at energies below the 1s resonance energy ($< 2.0$ eV). These calculations are consistent with experimental observations in similar systems [33, 34, 38].

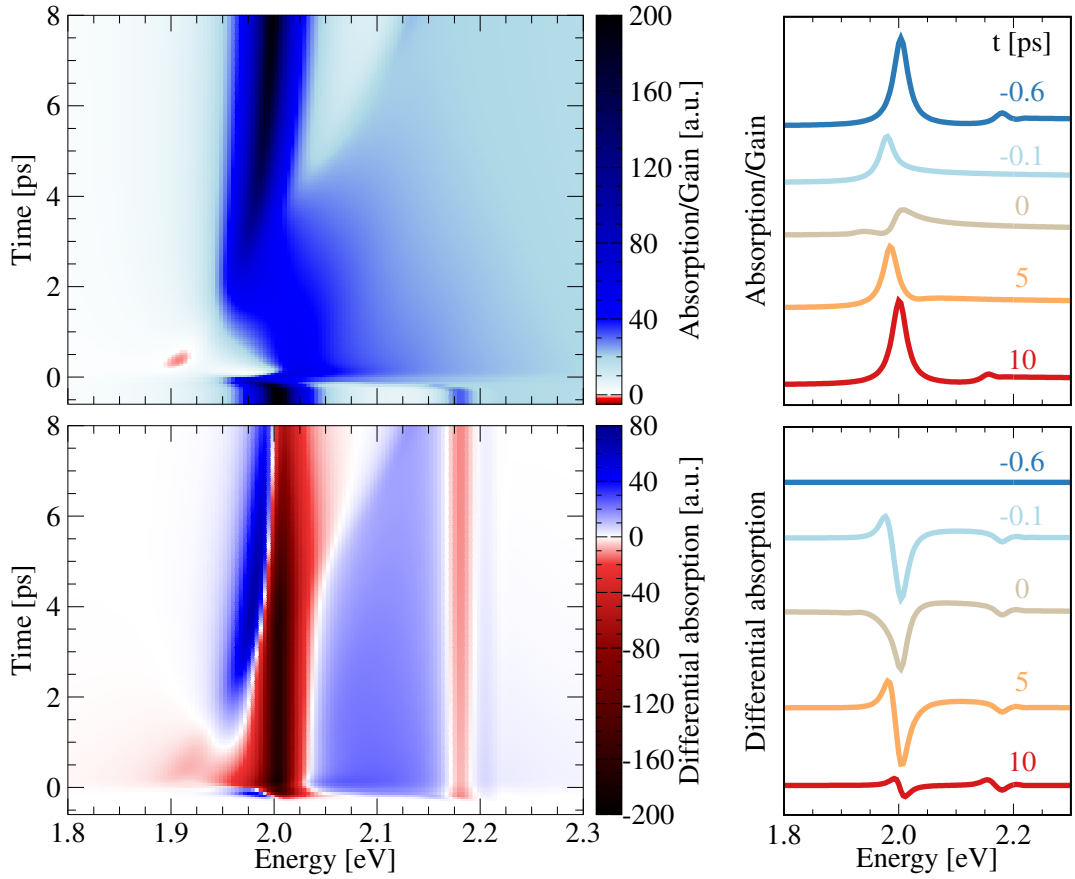


Figure 3.2: **Temporal evolution of the optical absorption.** Top: colormap (left) and timesnaps (right) of the optical absorption as a function of energy. Bottom: colormap (left) and timesnaps (right) of the differential absorption as a function of energy.

# Chapter 4

# Exciton diffusion

In the previous section the time- and energy-resolved dynamics of coherent exciton properties caused by the optical excitation of a large carrier population has been studied. However, the dynamics of long-lived incoherent excitons dominate important processes such as radiative recombination and diffusion. While the incoherent-exciton dynamics in momentum space – formation, thermalization and recombination – has been intensively studied in the last years [8, 30, 33, 39–42], fundamental spatial phenomena such as diffusion has remained in the dark. Besides initial reports [15–18], recent experimental studies show efficient exciton propagation at room temperature [19] and strong density dependence of the diffusion coefficient and the formation of spatial halos in the photoluminescence profile at elevated excitation densities [20]. While the latter is expected to arise from strong non-equilibrium effects, the underlying elementary processes are not clear. In order to unveil the mechanisms behind non-linear exciton diffusion and halo formation, the spatially-resolved microscopic theory presented in the theory section is used.

In the system considered here, strong non-equilibrium is expected to appear at strong excitation conditions due to Auger recombination. Through Auger scattering, one exciton can decay and transfer its energy and momentum to another exciton. Due to the large bandgap of TMDs (about 2 eV), a large amount of optical phonons will be emitted during the relaxation of these high-energy Auger-scattered excitons. The substantial number of non-equilibrium phonons will induce a heating of the excitonic system through phonon reabsorption. In order to take these processes into account Auger recombination is introduced on a semi-phenomenological level with the recombination rate $r_A N$, where $N$ is the exciton density and $r_A$ the Auger recombination coefficient – which can be measured in experiments [16, 17, 20]. Moreover, the phonon emission occuring during the relaxation of high-energy excitons is described by the rate $\alpha = 2\pi\varepsilon_{\mathrm{X}} r_A (\varepsilon_{\mathrm{op}} q_c^2)^{-1}$, which includes the ratio between the energy of excitons $\varepsilon_{\mathrm{X}}$ and optical phonons $\varepsilon_{\mathrm{op}}$, and the cut-off momentum $q_c$ up to which phonons are emitted. The equations of motion for excitons

$N_{\mathbf{Q}}$ and optical phonons $n_{\mathbf{q}}$ in this system can thus be written as:

$$\begin{aligned}\dot{N}_{\mathbf{Q}}(\mathbf{r},t) = &-\mathbf{v}_{\mathbf{Q}} \cdot \nabla_{\mathbf{r}} N_{\mathbf{Q}}(\mathbf{r},t) - r_A N_{\mathbf{Q}}(\mathbf{r},t) N(\mathbf{r},t) \\ &+ \Gamma^{\text{in}}_{\mathbf{Q}}(\mathbf{r},t) - \Gamma^{\text{out}}_{\mathbf{Q}}(\mathbf{r},t) N_{\mathbf{Q}}(\mathbf{r},t) \end{aligned} \tag{4.1}$$

$$\begin{aligned}\dot{n}_{\mathbf{q}}(\mathbf{r},t) = &\,\Gamma^{\text{em}}_{\mathbf{q}}(\mathbf{r},t)\,(1 + n_{\mathbf{q}}(\mathbf{r},t)) - \Gamma^{\text{abs}}_{\mathbf{q}}(\mathbf{r},t) n_{\mathbf{q}}(\mathbf{r},t) \\ &+ \alpha N^2(\mathbf{r},t) - \kappa \left(n_{\mathbf{q}}(\mathbf{r}) - n^0_{\mathbf{q}}\right) \end{aligned} \tag{4.2}$$

with $\mathbf{v}_{\mathbf{Q}} = \hbar \mathbf{Q} M_X^{-1}$ as the exciton velocity, $\kappa$ as the phonon decay rate, $n^0_{\mathbf{q}}$ as the equilibrium phonon number (described by a Bose distribution), and the exciton-phonon scattering rates $\Gamma^i_{\mathbf{Q}}$ being computed consistently according to the second-order Born-Markov approximation [30, 41]. Solving this system of equations provides access to the exciton spatio-temporal dynamics at different excitation densities. The optical excitation enters here as the initial spatial width and peak density of excitons described by a Gaussian in real space and a Boltzmann distribution in reciprocal space. Although this microscopic model applies to any two-dimensional material, parameters for $WS_2$ are used here [14, 20, 43].

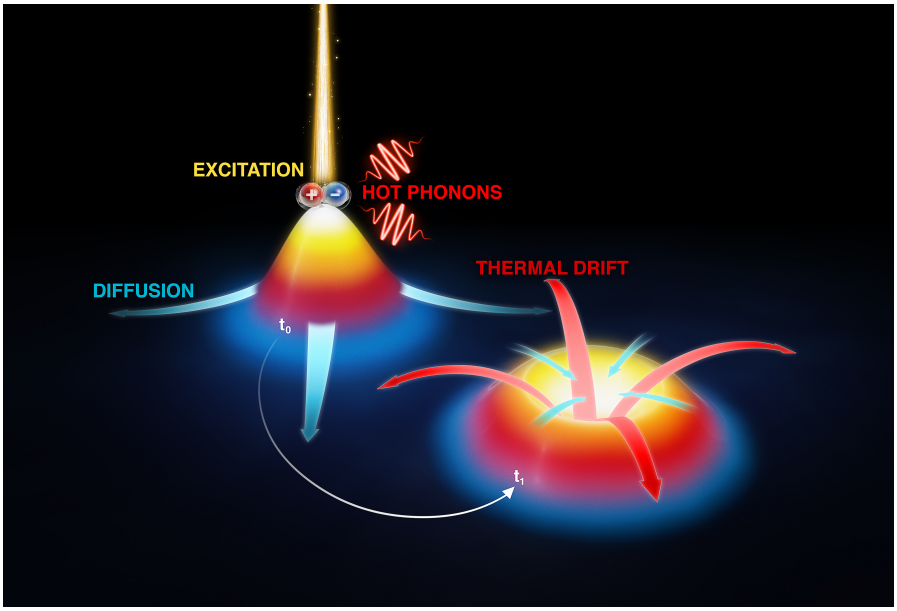


Figure 4.1: **Exciton diffusion and halo formation**. Excitons are locally generated by an optical Gaussian excitation and start diffusing to homogenize the spatial distribution ($t_0 \rightarrow t_1$). Through Auger recombination and relaxation by hot-phonon emission, a long-lived temperature gradient is formed in the excitonic system (color gradient). This gradient causes excitons to leave the excited region through a thermal drift resulting in the formation of spatial rings (halos).

## 4.1 Conventional diffusion

Figure 4.2 shows the exciton spatio-temporal dynamics calculated in the low-excitation regime ($n_0 = 10^9\,\mathrm{cm}^{-2}$). Subfigure (a) shows the exciton Wigner function in real- and momentum-space along the x-coordinate for four fixed times. As one can see, the distribution broadens in space as a result of excitons propagating with velocity $\mathbf{v_Q}$ and quickly thermalizing by scattering with phonons. This spatial broadening can be better visualized in the spatial profiles of the (momentum-integrated) exciton density (subfigure (b)). Furthermore, the spatial variance $w^2$ of the exciton density has a linear time dependence.

These observations are in agreement with Fick's law of diffusion for the exciton current $\mathbf{j}(\mathbf{r},t) = -D\nabla N(\mathbf{r},t)$ with the diffusion coefficient $D$ [44]. Using the continuity equation $\dot{N}(\mathbf{r},t) = -\nabla\cdot\mathbf{j}(\mathbf{r},t) = D\nabla^2 N(\mathbf{r},t)$ – if recombination is neglected –, one can find the solution $N(\mathbf{r},t) = N_0(4\pi Dt)^{-1}\exp\left(-\frac{\mathbf{r}^2}{w^2(t)}\right)$, with $w^2(t) = w_0^2+4Dt$ corresponding to the spatial variance. At low excitation densities, the linear time-dependence of the variance is fulfilled and the diffusion coefficient is extracted to be $2\,\mathrm{cm}^2\mathrm{s}^{-1}$. However, note in subfigure (c) that the variance is no longer linear in time and hence does not fulfill the standard Fick law of diffusion. Nevertheless, the slope of the variance increases with the excitation density, and an effective diffusion coefficient can be extracted, e.g. $20\,\mathrm{cm}^2\mathrm{s}^{-1}$ at $n_0 = 10^{12}\,\mathrm{cm}^{-2}$ The fact that the slope becomes smaller at longer times suggests that excitons move faster in the excited region and then slow once they leave this region. It will be shown in the next section that this behaviour is a result of a strong spatial gradient in the exciton temperature.

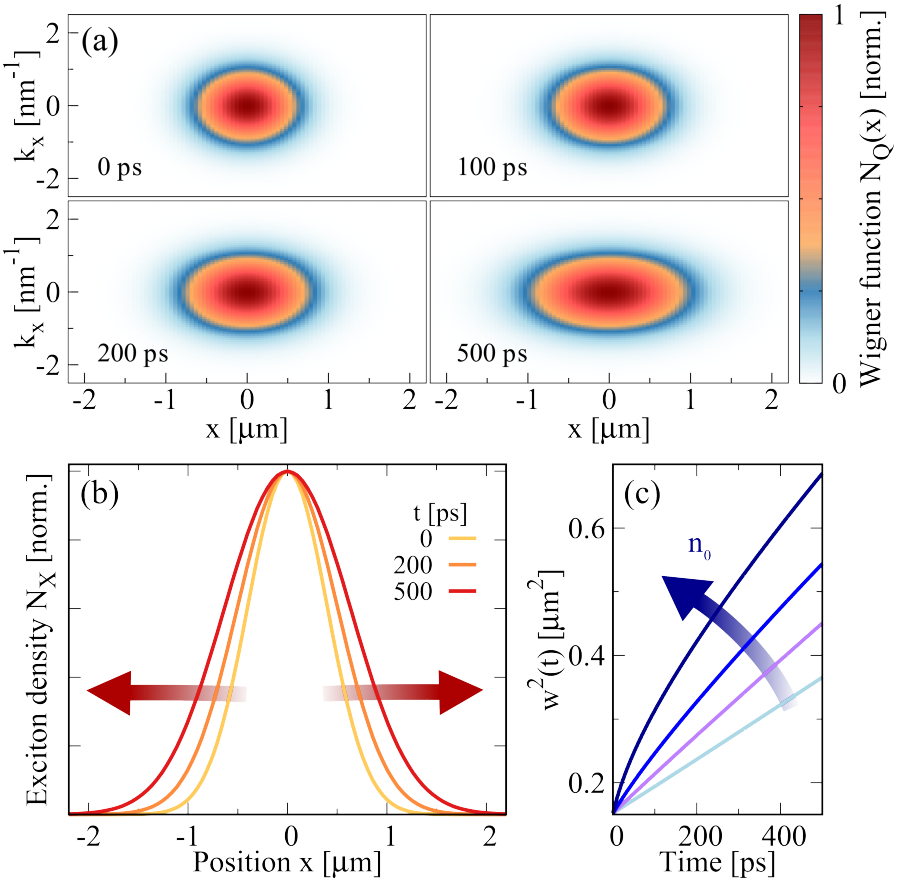


Figure 4.2: **Exciton diffusion in low-excitation regime**. (a) Phase-space representation of the normalized exciton Wigner function at different times for an initial exciton density of $10^9\,\mathrm{cm}^{-2}$. (b) Spatial distribution of the momentum-integrated exciton density at different times. (c) Spatial variance of the exciton density for different initial densities ($10^9$, $10^{10}$, $3 \times 10^{10}$, and $10^{11}\,\mathrm{cm}^{-2}$).

## 4.2 Thermal effects and halo formation

In order to investigate the origin of the density-dependent increase of the diffusion coefficient and the non-linear behaviour of the exciton spatial variance, the system is studied now in the high-excitation regime ($n_0 = 10^{12}\,\mathrm{cm}^{-2}$). Although this density is high enough for Auger scattering to become significant, it still is one order of magnitude away from the Mott transition, where carriers dominate the dynamics of the system [33, 45]. In Figure 4.3 (a) the Wigner representation of the exciton occupation is shown at four different times. In contrast to the low-density case, one can observe here an apparent accumulation of excitons at low momenta outside the central region a few picoseconds after the excitation. This is a result of a broader distribution in momentum space in the central excited region, which corresponds to a higher effective temperature. This temperature gradient induces an efficient thermal drift that leads to the evolution of the initial Gaussian profile into a super-Gaussian distribution followed by the formation of spatial rings (subfigure (b)). The heating of excitons in the central region (blue-shaded curve in subfigure (b)) is a direct consequence of the large phonon density in this region (subfigure (c)). When excitons undergo Auger recombination, the high-energy scattered excitons relax by emitting a vast amount of optical phonons, which are then reabsorbed, resulting in an effective heating of the exciton distribution. As the excitation density is increased these effects become more pronounced, and diffusion can not be described by the standard Fick law anymore.

Nevertheless, the expression for the current (4.1) can be generalized to account for gradients in the density $N$ and in the temperature $T_X$ of excitons. Within a relaxation time approximation with $\tau_{\mathbf{Q}}^{-1} = \Gamma_{\mathbf{Q}}^{\mathrm{in}} + \Gamma_{\mathbf{Q}}^{\mathrm{out}}$, the equation of motion for the exction spatio-temporal dynamics – neglecting recombination – can be written as $\dot{N}_{\mathbf{Q}}^0(\mathbf{r},t) = -\mathbf{v}_{\mathbf{Q}} \cdot \nabla N_{\mathbf{Q}}^0(\mathbf{r},t) - \tau_{\mathbf{Q}}^{-1} N_{\mathbf{Q}}^1(\mathbf{r},t)$, where $N^1$ is a small deviation from the equilibrium exciton distribution $N^1$. Here it has been assumed that $N^1$ is stationary in the timescale of diffusion and that its spatial gradients are weak. From this expression, $N^1$ can be described in function of $N^0$ in order to find an expression for the current:

$$\mathbf{j}(\mathbf{r},t) = \sum_{\mathbf{Q}} \mathbf{v}_{\mathbf{Q}} N_{\mathbf{Q}}^1(\mathbf{r},t) = -\sum_{\mathbf{Q}} \tau_{\mathbf{Q}} \mathbf{v}_{\mathbf{Q}} \mathbf{v}_{\mathbf{Q}} \cdot \nabla N_{\mathbf{Q}}^0(\mathbf{r},t) \tag{4.3}$$

Assuming that excitons can be described in equilibrium by a Boltzmann distribution $N_{\mathbf{Q}}^0(\mathbf{r},t) = 2\pi\hbar N(\mathbf{r},t)[m k_B T_X(\mathbf{r},t)]^{-1} \exp\left(-\frac{\varepsilon_Q}{k_B T_X(\mathbf{r},t)}\right)$, the gradient $\nabla N_{\mathbf{Q}}^0(\mathbf{r},t)$ can be expressed in terms of the density and the temperature, resulting in an expression for the current

$$\mathbf{j}(\mathbf{r},t) = -D\nabla N(\mathbf{r},t) - \sigma s \nabla T_X(\mathbf{r},t) \tag{4.4}$$

that accounts for gradients in the density and the temperature, with the conductivity $\sigma$ and the Seebeck coefficient $s$ fulfilling

$$\sigma s = (2k_B T_X^2)^{-1} \sum_{\mathbf{Q}} \tau_{\mathbf{Q}} v_{\mathbf{Q}}^2 \left(\varepsilon_{\mathbf{Q}} - k_B T_X\right) N_{\mathbf{Q}}^0 \approx \tau k_B N M_X^{-1} \tag{4.5}$$

and the diffusion coefficient

$$D = (2N)^{-1} \sum_{\mathbf{Q}} \tau_{\mathbf{Q}} v_{\mathbf{Q}}^2 N_{\mathbf{Q}}^0 \approx \tau k_B T_X M_X^{-1} \tag{4.6}$$

Note that an additional term is obtained that accounts for thermal drift (or Seebeck effect). According to this expression, excitons propagate in space to reduce any spatial non-uniformity in the density or temperature. When a temperature gradient is created excitons move out of the central hot region towards colder regions. A moderate gradient will result in a flattening of the Gaussian spatial profile of the exciton distribution. A sufficiently strong temperature gradient will be more effective in inducing the depletion of the hot region than diffusion in refilling it, thus leading to the formation of a spatial ring (see Fig. 4.1).

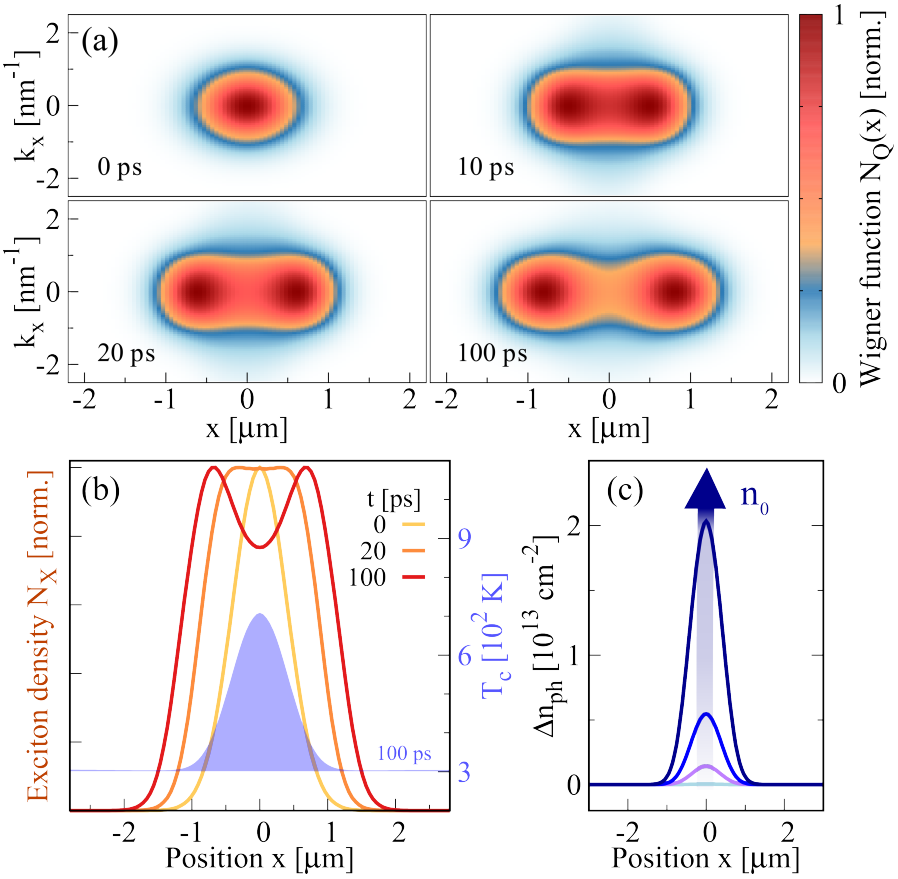


Figure 4.3: **Non-linear exciton diffusion and halo formation in the high-excitation regime**. (a) Phase-space representation of the normalized exciton Wigner function at different times for the initial exciton density of $n_0 = 10^{12}\,\mathrm{cm}^{-2}$. (b) Spatial distribution of the momentum-integrated exciton density at different times along the exciton temperature at 100 ps after the excitation (blue shaded curve). (c) Spatial profile of the excess optical phonon density at 100 ps for different initial densities ($10^{10}$, $10^{11}$, $3 \times 10^{11}$, and $10^{12}\,\mathrm{cm}^{-2}$).

## 4.3 Photoluminescence and experimental comparison

Although in the previous sections exciton diffusion has been studied, the directly experimentally accessible quantity is photoluminescence intensity. Photoluminescence is given by radiative recombination of excitons in the light cone (i.e. with zero momentum). However, the excitons considered correspond to the most populated state in $WS_2$, which has a finite momentum because it consists of a hole in the K-valley bound to an electron in the Λ-valley [31, 41, 46–49]. Nevertheless, intervalley thermal equilibrium can be assumed in the exciton distribution to determine the exciton occupation in the light cone and extract the photoluminescence.

The theoretical calculations are shown in Figure 4.4 together with experimental measurements performed by the group of Alexey Chernikov (Regensburg, Germany) [50]. The figure shows an excellent qualitative agreement between the theoretical prediction and the experimental observation. There is a clear transition from a Gaussian to a super-Gaussian profile followed by the formation of halos in the photoluminescence. An equally good agreement is observed in the formation and evolution of the halos, with the formation time ranging from tens to hundreds of picoseconds and the halo diameter following a sub-linear time evolution. Note that the halo formation time is shorter at higher excitations due to more excitons leading to a stronger heating. In the experimental measurements a slower diffusion coefficient is observed in comparison with the theoretical prediction (note that the spatial distribution is narrower). This can be caused by scattering with defects [16]. This smaller diffusion coefficient implies that a weaker temperature gradient is strong enough to overcome the diffusion force and induce the formation of halos at densities lower than the predicted here.

Subfigure (e) shows the predicted effective exciton diffusion coefficient $D_{\text{eff}}$ as a function of initial exciton density. At low densities $D_{\text{eff}}$ remains constant. At higher densities Auger scattering becomes significant and the diffusion coefficient increases strongly – in agreement with previous experimental observations [20]. There are three contributions to the increase of the diffusion coefficient: (1) thermal drift of excitons out of the central region, (2) higher averaged squared exciton velocity (higher temperature) with a constant lattice temperature (scattering with acoustic phonons does not become stronger), and (3) density-dependent Auger recombination that is stronger in the more-populated center and makes the distribution effectively broader.

The increased optical phonon density has an experimentally-accessible effect in the linewidth of the photoluminescence peak due to increased exciton-phonon scattering rates [31, 51]. Subfigure (e) also shows the predicted linewidth change at the excited spot. This quantity is negligible at densities up to $10^{11}\,\text{cm}^{-2}$ and

it increases exponentially at higher densities. Nevertheless, a linewidth increase caused by exciton-exciton scattering is also expected to contribute [13], but it is not included in this work. The experimental measurement of the linewidth increase in space and time would give access to the dynamics of hot phonons.

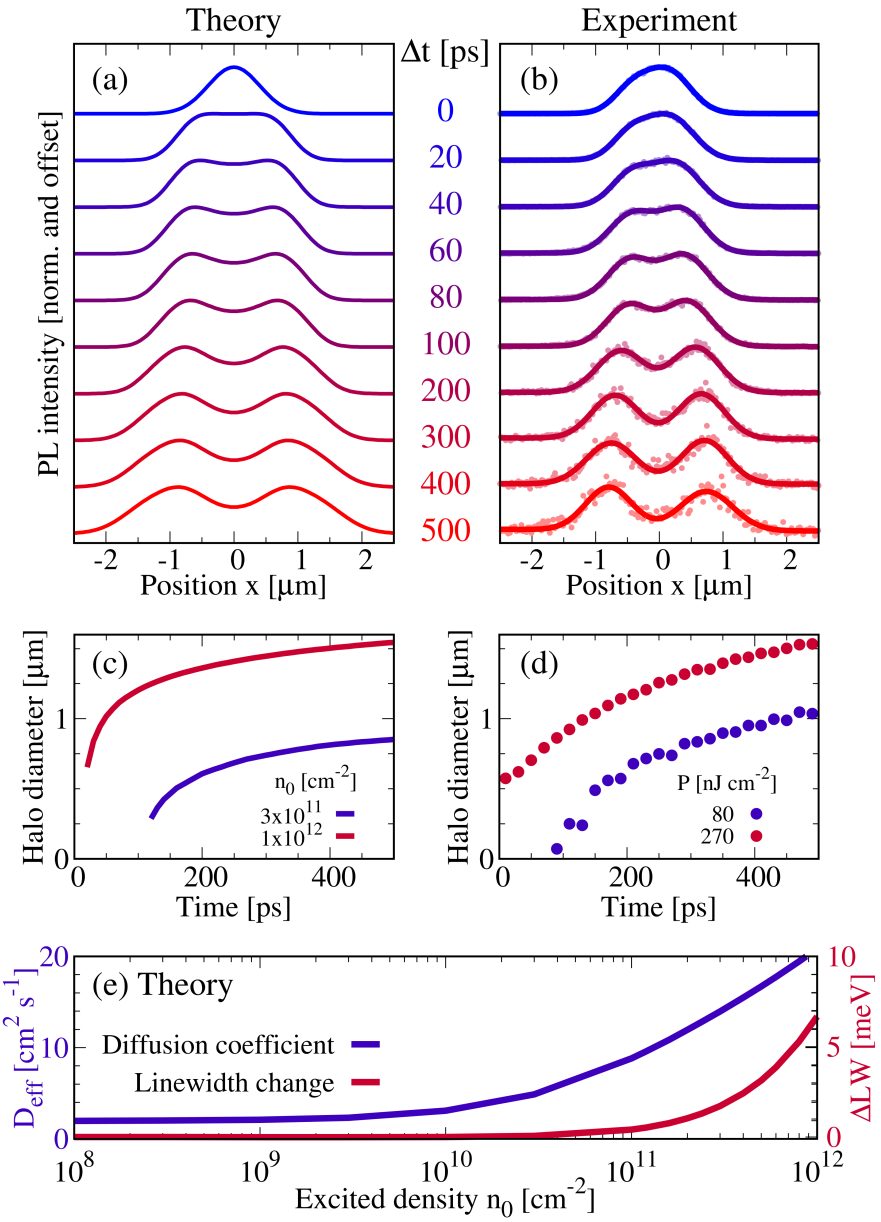


Figure 4.4: **Direct theory-experiment comparison.** (a)-(b) Theoretically predicted and experimentally measured temporal and spatial evolution of photoluminescence for an initially excited exciton density of $10^{12}$ cm$^{-2}$ and an excitation energy density of 270 nJcm$^{-2}$, respectively. (c)-(d) Theory-experiment comparison of the halo formation for two different initial exciton densities. (e) Theoretical prediction of density dependence of the effective diffusion coefficient (blue line) and the linewidth change at the excitation spot evaluated 100 ps after the excitation (red line).

# Chapter 5

# Conclusions

A quantum-mechanical theoretical framework based on the density matrix formalism has been introduced to microscopically describe dynamics in atomically thin TMDs. On the one hand, semiconductor Bloch equations and the Wannier equation have been presented and combined in order to obtain access to energy- and time-resolved dynamics of charge-carriers, exciton properties and optical absorption. It has been found that under strong excitation a large carrier density bleaches the excitonic properties and thus the optical absorption of TMDs due to Pauli-blocking and many-particle dielectric screening. Particularly, the time-resolved theory presented here provides a framework for understanding fundamental phenomena in pump-probe experiments.

On the other hand, the Wigner representation has been introduced to extend the equations of motion and be able to trace the way of particles in energy, space and time. Applying this to excitons allowed to understand and unveil the mechanisms behind very recent experimental observations reporting the appearance of halos in the photoluminescence at high excitation densities. It has been shown here that at high excitation densities Auger recombination becomes significant. When excitons undergo Auger recombinations, ones recombine while others gain energy and momentum. The high-energy excitons then relax through scattering with optical phonons. Due to the large exciton resonance energy, the emission of optical phonons can be enormous, resulting in hot-phonon effects. The reabsorption of these hot phonons originates a strong gradient in the exciton temperature, which causes thermal drift (Seebeck effect) of excitons out of the excited region to be very significant. In the end, this results in the evolution of the initial Gaussian into a ring-shaped profile of the exciton density. Since the photolumienscence is mainly given by the exciton population and at room temperature and the timescales of diffusion there is inter-valley thermal equilibrium, this corresponds to a halo shape of the photoluminescence. This work [50] has provided a microscopic description of this intruiging phenomenon and theoretical predictions on the density-dependence

of exciton diffusion. In conclusion, both parts of this thesis contributed to a better understanding of TMDs and provided a theoretical framework to further study related phenomena.

There are clear natural steps that could be followed to extend the work done here. First, combining the two sections would allow to study spatio-temporal pump-probe experiments, which could allow to trace the way of electrons and holes in space, energy and time. Additional work could also be more focused into device application. In this sense, the effect of an internal electric field (pn junction) or of an external electric field would be very important points to study for the application of TMDs in optoelectronic devices such as photodetectors, LEDs or solar cells. Moreover, the knowledge acquired here could be extended to the novel fields of van der Waals heterostructures and Moiré physics. Van der Waals heterostructures consist of at least two layers of two dimensional materials. When one of the layers is twisted with respect to the other, a super-lattice with a Moiré pattern appears, giving rise to fascinating phenomena which strongly depend on the twisting angle [52]. This new tunnability degree of freedom gives name to a field that is expected to become exceptional and outstanding in the near future: twisttronics.

# References


1. Novoselov, K. S. *et al.* Electric field effect in atomically thin carbon films. *science* **306,** 666–669 (2004).
2. Neto, A. C., Guinea, F., Peres, N. M., Novoselov, K. S. & Geim, A. K. The electronic properties of graphene. *Reviews of modern physics* **81,** 109 (2009).
3. Novoselov, K. S. *et al.* Two-dimensional atomic crystals. *Proceedings of the National Academy of Sciences* **102,** 10451–10453 (2005).
4. Fiori, G. *et al.* Electronics based on two-dimensional materials. *Nature nanotechnology* **9,** 768 (2014).
5. Ferrari, A. C. *et al.* Science and technology roadmap for graphene, related two-dimensional crystals, and hybrid systems. *Nanoscale* **7,** 4598–4810 (2015).
6. Mounet, N. *et al.* Two-dimensional materials from high-throughput computational exfoliation of experimentally known compounds. *Nature nanotechnology* **13,** 246 (2018).
7. Wang, Q. H., Kalantar-Zadeh, K., Kis, A., Coleman, J. N. & Strano, M. S. Electronics and optoelectronics of two-dimensional transition metal dichalcogenides. *Nature nanotechnology* **7,** 699 (2012).
8. Mueller, T. & Malic, E. Exciton physics and device application of two-dimensional transition metal dichalcogenide semiconductors. *npj 2D Materials and Applications* **2,** 29 (2018).
9. Mak, K. F., Lee, C., Hone, J., Shan, J. & Heinz, T. F. Atomically thin MoS 2: a new direct-gap semiconductor. *Physical review letters* **105,** 136805 (2010).
10. Steinhoff, A., Rosner, M, Jahnke, F., Wehling, T. O. & Gies, C. Influence of excited carriers on the optical and electronic properties of MoS2. *Nano letters* **14,** 3743–3748 (2014).
11. Haug, H. & Koch, S. W. *Quantum Theory of the Optical and Electronic Properties of Semiconductors: Fivth Edition* (World Scientific Publishing Company, 2009).

12. Kira, M & Koch, S. W. Many-body correlations and excitonic effects in semiconductor spectroscopy. *Progress in quantum electronics* **30,** 155–296 (2006).

13. Kira, M. & Koch, S. W. *Semiconductor quantum optics* (Cambridge University Press, 2011).

14. Jin, Z., Li, X., Mullen, J. T. & Kim, K. W. Intrinsic transport properties of electrons and holes in monolayer transition-metal dichalcogenides. *Physical Review B* **90,** 045422 (2014).

15. Kato, T. & Kaneko, T. Transport Dynamics of Neutral Excitons and Trions in Monolayer WS2. *ACS nano* **10,** 9687–9694 (2016).

16. Yuan, L., Wang, T., Zhu, T., Zhou, M. & Huang, L. Exciton dynamics, transport, and annihilation in atomically thin two-dimensional semiconductors. *The journal of physical chemistry letters* **8,** 3371–3379 (2017).

17. Mouri, S. *et al.* Nonlinear photoluminescence in atomically thin layered WSe 2 arising from diffusion-assisted exciton-exciton annihilation. *Physical Review B* **90,** 155449 (2014).

18. Kumar, N. *et al.* Exciton diffusion in monolayer and bulk MoSe 2. *Nanoscale* **6,** 4915–4919 (2014).

19. Cadiz, F *et al.* Exciton diffusion in WSe2 monolayers embedded in a van der Waals heterostructure. *Applied Physics Letters* **112,** 152106 (2018).

20. Kulig, M. *et al.* Exciton diffusion and halo effects in monolayer semiconductors. *Physical review letters* **120,** 207401 (2018).

21. Glazov, M. Phonon wind and drag of excitons in monolayer semiconductors. *arXiv preprint arXiv:1905.01621* (2019).

22. Berghäuser, G. & Malic, E. Analytical approach to excitonic properties of MoS 2. *Physical Review B* **89,** 125309 (2014).

23. Rytova, N. S. The screened potential of a point charge in a thin film. *Moscow University Physics Bulletin* **3,** 18 (1967).

24. Keldysh, L. V. Coulomb interaction in thin semiconductor and semimetal films. *Soviet Journal of Experimental and Theoretical Physics Letters* **29,** 658 (June 1979).

25. Malic, E. & Knorr, A. *Graphene and Carbon Nanotubes: Ultrafast Optics and Relaxation Dynamics* (John Wiley & Sons, 2013).

26. Wigner, E. On the Quantum Correction For Thermodynamic Equilibrium. *Phys. Rev.* **40,** 749–759 (5 1932).

27. Hess, O. & Kuhn, T. Maxwell-Bloch equations for spatially inhomogeneous semiconductor lasers. I. Theoretical formulation. *Physical Review A* **54,** 3347 (1996).

28. Rossi, F. & Kuhn, T. Theory of ultrafast phenomena in photoexcited semiconductors. *Reviews of Modern Physics* **74,** 895 (2002).

29. Katsch, F., Selig, M., Carmele, A. & Knorr, A. Theory of Exciton–Exciton Interactions in Monolayer Transition Metal Dichalcogenides. *physica status solidi (b)* **255,** 1800185 (2018).

30. Brem, S., Selig, M., Berghaeuser, G. & Malic, E. Exciton Relaxation Cascade in two-dimensional Transition Metal Dichalcogenides. *Scientific reports* **8,** 8238 (2018).

31. Selig, M. *et al.* Excitonic linewidth and coherence lifetime in monolayer transition metal dichalcogenides. *Nature communications* **7,** 13279 (2016).

32. Knorr, A, Hughes, S, Stroucken, T & Koch, S. W. Theory of ultrafast spatio-temporal dynamics in semiconductor heterostructures. *Chemical physics* **210,** 27–47 (1996).

33. Chernikov, A., Ruppert, C., Hill, H. M., Rigosi, A. F. & Heinz, T. F. Population inversion and giant bandgap renormalization in atomically thin WS 2 layers. *Nature Photonics* **9,** 466 (2015).

34. Pogna, E. A. *et al.* Photo-induced bandgap renormalization governs the ultrafast response of single-layer MoS2. *ACS nano* **10,** 1182–1188 (2016).

35. Ceballos, F., Cui, Q., Bellus, M. Z. & Zhao, H. Exciton formation in monolayer transition metal dichalcogenides. *Nanoscale* **8,** 11681–11688 (2016).

36. Chernikov, A. *et al.* Electrical tuning of exciton binding energies in monolayer WS 2. *Physical review letters* **115,** 126802 (2015).

37. Ruppert, C., Chernikov, A., Hill, H. M., Rigosi, A. F. & Heinz, T. F. The role of electronic and phononic excitation in the optical response of monolayer WS2 after ultrafast excitation. *Nano letters* **17,** 644–651 (2017).

38. Sie, E. J. *et al.* Observation of exciton redshift–blueshift crossover in monolayer WS2. *Nano letters* **17,** 4210–4216 (2017).

39. Wang, G. *et al.* Colloquium: Excitons in atomically thin transition metal dichalcogenides. *Reviews of Modern Physics* **90,** 021001 (2018).

40. Steinhoff, A. *et al.* Nonequilibrium carrier dynamics in transition metal dichalcogenide semiconductors. *2D Materials* **3,** 031006 (2016).

41. Selig, M. *et al.* Dark and bright exciton formation, thermalization, and photoluminescence in monolayer transition metal dichalcogenides. *2D Materials* **5,** 035017 (2018).

42. Merkl, P *et al.* Ultrafast transition between exciton phases in van der Waals heterostructures. *Nature materials,* 1 (2019).

43. Kormányos, A. *et al.* k· p theory for two-dimensional transition metal dichalcogenide semiconductors. *2D Materials* **2,** 022001 (2015).

44. Pathria, R. & Beale, P. D. in *Statistical Mechanics (Third Edition)* (eds Pathria, R. & Beale, P. D.) Third Edition, 583 –635 (Academic Press, Boston, 2011). ISBN: 978-0-12-382188-1. doi:https://doi.org/10.1016/B978-0-12-382188-1.00015-3. <http://www.sciencedirect.com/science/article/pii/B9780123821881000153>.

45. Steinhoff, A. *et al.* Exciton fission in monolayer transition metal dichalcogenide semiconductors. *Nature communications* **8,** 1166 (2017).

46. Malic, E. *et al.* Dark excitons in transition metal dichalcogenides. *Physical Review Materials* **2,** 014002 (2018).

47. Deilmann, T. & Thygesen, K. S. Finite-momentum exciton landscape in mono-and bilayer transition metal dichalcogenides. *2D Materials* (2019).

48. Berghäuser, G. *et al.* Mapping of the dark exciton landscape in transition metal dichalcogenides. *Physical Review B* **98,** 020301 (2018).

49. Feierabend, M., Berghäuser, G., Knorr, A. & Malic, E. Proposal for dark exciton based chemical sensors. *Nature communications* **8,** 14776 (2017).

50. Perea-Causin, R. *et al.* Exciton propagation and halo-formation in two-dimensional materials. *arXiv preprint arXiv:1906.02084* (2019).

51. Brem, S. *et al.* Intrinsic Lifetime of Higher Excitonic States in Tungsten Diselenide Monolayers. *arXiv preprint arXiv:1904.04729* (2019).

52. Yu, H., Liu, G.-B., Tang, J., Xu, X. & Yao, W. Moiré excitons: From programmable quantum emitter arrays to spin-orbit–coupled artificial lattices. *Science advances* **3,** e1701696 (2017).